Supporting Information

Seizing Gaseous Fe^{2+} to Densify O_2-Accessible $Fe–N_4$ Active Sites for High-Performance Proton Exchange Membrane Fuel Cells

Shu-Hu Yin,[a] Shuang-Li Yang,[a] Gen Li,[a] Guang Li,[a] Bin-Wei Zhang,[a] Chong-Tai Wang,[b] Ming-Shu Chen,[a] Hong-Gang Liao,[a] Jian Yang,[a]* Yan-Xia Jiang[a]* and Shi-Gang Sun[a]*

[a] S. Yin, S. Yang, G. Li, G. Li, B. Zhang, Prof. S. Chen, Prof. G. Liao, Dr. J. Yang, Prof. Y. Jiang*, Prof. S. Sun**
State Key Laboratory of Physical Chemistry of Solid Surfaces, Department of Chemistry, College of Chemistry and Chemical Engineering
Xiamen University
Xiamen, 361005, People's Republic of China
E-mail: wjianyang@outlook.com, yxjiang@xmu.edu.cn, sgsun@xmu.edu.cn

[b] Prof. C. Wang
College of Chemistry and Chemical Engineering, Hainan Normal University, Key Laboratory of Electrochemical Energy Storage and Energy Conversion of Hainan Province, Haikou 571158, People's Republic of China

Experimental Section

Synthesis.

Chemicals: Zinc nitrate hexahydrate ($Zn(NO_3)_2 \cdot 6H_2O$, ≥ 99.0%), Iron(II) chloride tetrahydrate ($FeCl_2 \cdot 4H_2O$, ≥ 99.99%), 1,10-phenanthroline monohydrate (Phen), methanol solution, ethanol solution were purchased from Shanghai Chemical Reagents, China. 2-methylimidazole (2-mIm) was purchased from Alfa Aesar. De-ionized water with a specific resistance of 18.25 MΩ·cm was used. All reagents were of analytical grade and used as received without further purification.

Synthesis of the Zn-based zeolitic imidazolate framework (ZIF8): In a typical procedure, $Zn(NO_3)_2 \cdot 6H_2O$ (10 mmol, 2.975 g) and 2-mIm (80 mmol, 6.568 g) was dissolved by ultrasound for 5 minutes in 100 mL methanol separately, then $Zn(NO_3)_2$ solution was poured rapidly into 2-mIm solution. The mixture was stirred sharply for 16 h at room temperature. The as-obtained white ZIF8 precipitate was centrifuged and washed with methanol several times and dried in vacuum at 333 K for overnight.

Synthesis of NC: The powder of ZIF8 was placed in a tube furnace and then heated to 1273 K (5 $K \cdot min^{-1}$) for 1 h under flowing Ar atmosphere, followed by cooling down naturally to room temperature. The powder collected was labeled as NC.

Synthesis of NC/Phen: 1.0 g ZIF8 and regular 1,10-phenanthroline were dispersed in a solution of ethanol and deionized water with a volume ratio of 2:1. The mixture was magnetically stirred for 12 h at room temperature and then evaporated at 353 K oil bath. The dry powders were thoroughly ground and pyrolyzed under Ar at 1273 K (5 $K \cdot min^{-1}$) for 1 h and then naturally cooled to room temperature. The as-prepared black products were directly named NC/Phen.

Synthesis of Fe_g-NC and Fe_g-NC/Phen: A certain amount of $FeCl_2 \cdot 4H_2O$ was placed in the bottom of the quartz boat, the quartz fiber membrane was placed in the middle and 80 mg NC or NC/Phen was placed on the quartz fiber membrane. The furnace was heated up to a variety of temperatures with a ramping rate of 5 $K \cdot min^{-1}$ under Ar gas, and then held at 1023 K for 3 h. The samples were finally collected by slowly moving a small magnet ~0.5 cm above to remove Fe nanoparticles. The as-obtained black products were directly used without any post-treatment and labeled Fe_g-NC and Fe_g-NC/Phen, respectively.

Synthesis of Fe_I-NC/Phen: 80 mg NC/Phen was dispersed in 20 mL ethanol under sonication 30 min. The 5 mg $FeCl_2 \cdot 4H_2O$ in 10 mL ethanol was subsequently poured into NC/Phen solution. The mixture was stirred vigorously for 3 h at room temperature and then evaporated at 353 K oil bath. The dry powders were thoroughly ground and heated up 1173 K with a ramping rate of 5 $K \cdot min^{-1}$ for 1 h under Ar gas. The as-obtained black products were directly used without any post-treatment and labeled Fe_I-NC/Phen.

Physical characterizations.

Scanning electron microscopy (SEM) images were measured on Histachi S4800 operated at 15 kV. Transmission electron microscopy (TEM), high-resolution transmission electron microscopy (HR-TEM) measurements were performed on TECNAI F20 at an acceleration voltage of 200 kV. Scanning transmission electron microscopy (STEM), elemental mapping were taken on FEI Talos F200s at an acceleration voltage of 200 kV, high-angle annular dark-field scanning transmission electron microscope (HAADF-STEM) was carried out on FEI Themis Z instrument operated at 200 kV with cold filed-emission gun and aberration corrector, and the samples were prepared by dropping ethanol dispersion of samples onto copper microgrid. Atomic-resolution micrographs were obtained using FEI Titan Themis 60-300 operated at 200 kV. N_2 physisorption measurements were carried out on a Micromeritics Tristar 3020 Surface Area Analyzer. Prior to N_2 adsorption, the sample was dried under vacuum at 200 °C for 3 h. X-ray power diffraction (XRD) patterns were taken on a Rigaku Ultima IV diffractometer (Rigaku, Japan) with Cu Kα X-ray source. X-ray photoelectron spectroscopy (XPS) measurements were conducted on a PHI Quantun-2000 using Al Kα radiation (1846.6 eV) as the X-ray source. Binding energies reported herein are with reference to C (1s) at 284.5 eV. FTIR was performed on a Nicolet IS10 FTIR spectrophotometer on KBr pellets in the wavelength region of 4000−400 cm^{-1}. The concentration of Fe element in samples is determined by the ICP-MS (Perkin Elmer Nexion 300). The X-ray absorption spectra were collected on the beamline BL07A1 in NSRRC. The radiation was monochromatized by a Si (111) double-crystal monochromator. ^{57}Fe Mössbauer transmission spectra were recorded at room temperature using a conventional constant acceleration spectrometer (Wissel) with a γ-ray source of 25 mCi ^{57}Co in a rhodium matrix. The Fe K-edge XANES data were recorded in a transmission mode and analyzed using IFEFFIT program. Fe_2O_3, Fe foil and FePc were used as references. The obtained XAFS data was processed in Athena (version 0.9.26) for background, pre-edge line and post-edge line calibrations. Then Fourier transformed fitting was carried out in Artemis (version 0.9.26). The k^3 weighting, k-range of 3 – 12 $Å^{-1}$ and R range of 1 – ~3 Å were used for the fitting of standers, 2 – ~9 $Å^{-1}$ and R range of 1 – ~2.4 Å were used for the fitting of samples. The four parameters, coordination number, bond length, Debye-Waller factor and E_0 shift (CN, R, σ^2, ΔE_0) were fitted without anyone was fixed, constrained, or correlated. For Wavelet Transform analysis, the χ(k) exported from Athena was imported into the Hama Fortran code. The parameters were listed as follow: R range, 1 – 4 Å, k range, 0 – 13 $Å^{-1}$ for standers and for 0 – 11 $Å^{-1}$ samples; k weight, 2; and Morlet function with κ=10, σ=1 was used as the mother wavelet to provide the overall distribution. High Sensitivity Low Energy Ion Scattering Spectroscopy (HS-LEIS): Low Energy Ion Scattering Spectroscopy (LEIS) analysis is based on the energy of the backscattering ions (nobel gas ions at an energy of a few keV, like He^+, Ne^+, Ar^+ *etc*.) to determine the masses of the scattering surface atoms. The surface coverage of each element is proportional to the measured intensity. Compared with the conventional LEIS instrument, HS-LEIS (Qtac100) can achieve about 3000 times higher sensitivity. In order to minimize the damage to the surface, helium was selected as the ion source

with a kinetic energy of 3 keV, an ion flux of 6000 pA m^{-2}, and a spot size of 2 mm × 2 mm.

Electrochemical measurements.

All electrochemical curves were measured on a CHI 760e electrochemical workstation using three-electrode system. To prepare a homogeneous ink containing the catalyst, 6 mg of the catalyst was dispersed in 1 mL of solution containing 600 µL of isopropanol, 380 µL of ultrapure water and 20 µL of 5% Nafion solution under sonication for 30 min. The commercial 20 wt.% Pt/C sample was prepared by dispersing 1 mg of the catalyst in 1 mL of 0.05% Nafion solution. Then a certain volume of the catalyst ink was carefully dropped onto the polished glassy carbon rotating desk electrode (RDE, diameter is 5 mm, area is 0.196 cm^2) or rotating ring disk electrode (RRDE, diameter is 5.61 mm, area is 0.2475 cm^2), leading to a desirable catalyst loading. The absolute mass of the catalyst loading was 0.6 mg_{total} cm^{-2} for M-N-C and 0.012 mg_{Pt} cm^{-2} for Pt/C. This catalyst modified glassy carbon electrode, graphite rod, and a saturated calomel electrode (SCE) were used as the working electrode, counter electrode, and reference electrode, respectively. The potentials in this work were referred to reversible hydrogen electrode (RHE) potentials by using the conversion equation $E_{RHE} = E_{SCE} + 0.2415 + 0.059$ pH.

Oxygen reduction reaction (ORR) tests were performed at 30 °C in 0.1 M H_2SO_4 soluton. RRDE measurements were conducted by linear sweep voltammetry (LSV) with the potential range from 0.1 to 1.1 V vs. RHE at 900 rpm with a scan rate of 10 mV s^{-1}, while the ring electrode was held at 1.2 V vs. RHE. The number of electron transfer (n) and the percent of H_2O_2 were calculated by the following equations:

$$n = \frac{4 \times I_D}{I_D + {I_R}/{N}} \quad (1)$$

$$H_2O_2\,(\%) = \frac{200 \times {I_R}/{N}}{I_D + {I_R}/{N}} \quad (2)$$

where I_D is the disk current, I_R is the ring current, and N (0.37) is the current collection efficiency of the Pt ring.

The kinetic current densities (j_k) involved during the ORR process were determined by analyzing Koutecky-Levich (K-L) equation (3):

$$\frac{1}{j} = \frac{1}{j_k} + \frac{1}{j_L} \quad (3)$$

where j is the measured current density, j_L and j_k are the limiting and kinetic current densities.

ORR results were presented after subtractions of the currents measured in N_2-saturated 0.1 M H_2SO_4 solution to remove capacitive currents. The accelerated durability tests (ADTs) were performed at 303 K in O_2-saturated 0.1 M H_2SO_4 solution

by applying cyclic potential sweeps between 0.6-1.0 V vs. RHE at a sweep rate of 50 mV s^{-1} for 5000 cycles.

Quantification of active centers. The SD was obtained according to the previously reported nitrite reduction method by Kucernak ea al. Briefly, nitrite could interact with Fe metal centre to form stable poisoned adducts. The poisoned adducts could be stripped entirely in the region of 0.35 to −0.35 V (*vs.* RHE). The excess coulometric charge (Q_{strip}) associated with the stripping peak was proportional to the SD:

$$SD\ (mol\ g^{-1}) = \frac{Q_{strip}\ (C\ g^{-1})}{n_{strip}\ F\ (C\ mol^{-1})} \quad (4)$$

$$TOF\ (s^{-1}) = \frac{n_{strip}\ \Delta j_k\ (mA\ cm^{-2})}{Q_{strip}\ (C\ g^{-1})\ L_C\ (mg\ cm^{-2})} \quad (5)$$

where n_{strip} (=5) is the number of transferred electrons per stripped one nitrite. F is Faraday's constant. L_C was the catalyst loading (0.242 mg cm^{-2}). The catalysts were tested without further treatment.

PEMFCs tests. Membrane electrode assemblies (MEAs) were prepared using the hot-pressing method. The cathode ink was prepared by ultrasonic mixing of the desired amounts of Fe-NC catalysts, deionized water (0.2 mL), isopropanol (0.8 mL) and a Nafion solution (5 wt%) in an ice bath over 1h. The ink was directly deposited onto a gas diffusion layer (GDL, PTFE-pretreated Toray 060 carbon paper) at a catalyst loading of 3.5 mg cm^{-2}. The Nafion content in the cathode catalyst layer was nearly 50 wt%. The anode catalyst is 40 wt% Pt/C with a loading of 0.4 mg_{Pt} cm^{-2}. The MEA was fabricated by hot-pressing the as-prepared cathode together with an anode, a Nafion membrane (NRE 211), and a gasket at 403 K and 3 MPa for 2 min. The active area of the MEA was 2.1 × 2.1 cm^2. Polarization curves were obtained at 353 K using a Model 850e fuel cell test system (Scribner Associates, Inc.) in conjunction with a back pressure of 1 bar or 2 bar read at the cathode gauge. The H_2 and O_2 (air) flow rates were 0.3 L min^{-1} and 0.4 L min^{-1} at 100% RH during the polarization curve measurements.

Computational method

All spin-polarized computations have been carried out with the Vienna ab initio Simulation Package. The exchange correlation functional PBE has been applied in combination with the Van der Waals interaction, and the kinetic cut-off energy has been taken as 400 eV. The GGA+U method has been applied to account for the localized 3d orbitals of Fe center in the relevant FeN_4 structures, and the Hubbard U values has been chosen to be 3.4 eV. The Brillouin zones of the FeN_4-C8 and FeN_4-C10 structures have been sampled with 5×5×1 k-point mesh in the Monkhorst–Pack scheme. The distance between the periodic images of carbon layer is 20 Å. During the geometry optimization, the energy convergence criterion is 10^{-5} eV, and the final forces are less than 0.01 eV $Å^{-1}$. The dipole correction is included throughout this study. The O_2 adsorption energy has been calculated according to eqn (6):

$$E_{ads} = E_{*-O_2} - E_{*} - E_{O_2} \quad (6)$$

Where E_{*-O_2}, E_{*}, E_{O_2} are electronic energies related to the FeN_4 structure with O_2 adsorption, the FeN_4 structure and O_2 molecule. The free energy correction at temperature of 1023 K is carried out by the numerical frequency computation. Correspondingly, the reaction free energy (ΔG) is calculated by eqn (7):

$$\Delta G = \Delta E + \Delta ZPE - T\Delta S \quad (7)$$

where E, ZPE, and S represent ground state energy, zero point energy, and entropy, respectively. The free energy of exchange reaction from ZnN_4 to FeN_4 site is calculated according to the eqn (8):

$$FeCl_2 + ZnN_4 \rightarrow ZnCl_2 + FeN_4 \quad (8)$$

Supplementary figures

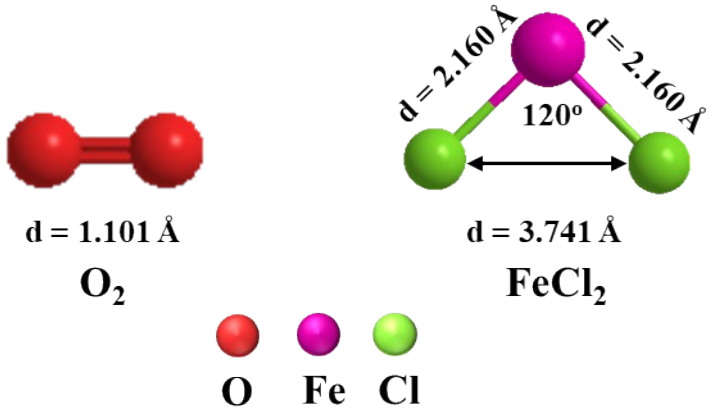

Fig. S1 The molecular diameters of O_2 and $FeCl_2$ molecules.

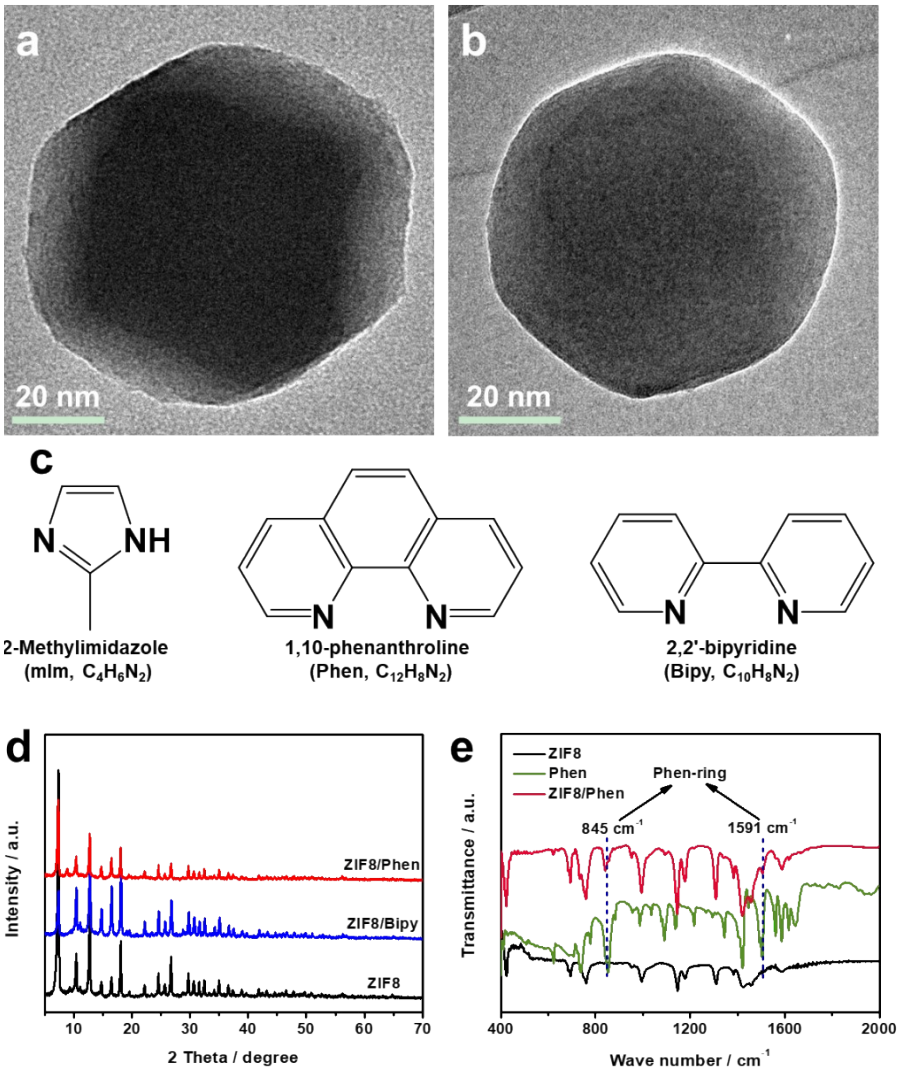

Fig. S2 TEM images of (a) the ZIF8 and (b) the ZIF8/Phen particles; (c) the molecular structure of mIm, Phen and Bipy. (d) XRD patterns of the ZIF8, ZIF8/Bipy and ZIF8/Phen precursors. (e) FTIR spectra of the ZIF8, Phen and ZIF8/Phen precursors.

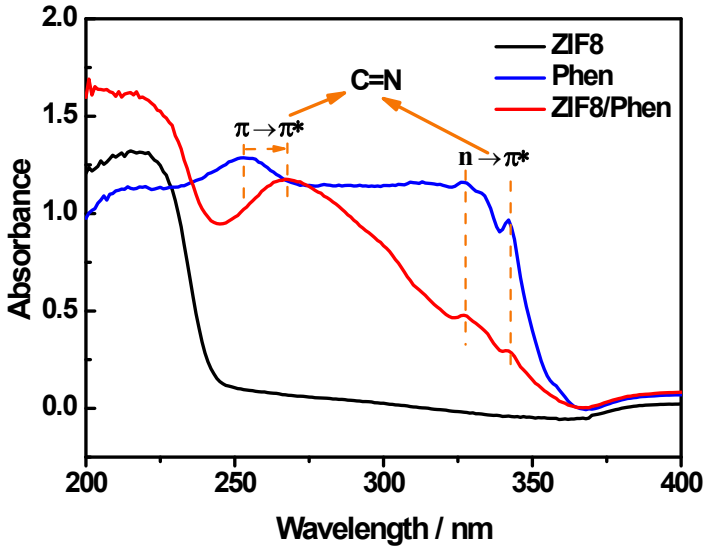

Fig. S3 Solid-state UV-Vis DRS analysis of the ZIF8, Phen, ZIF8/Phen precursors.

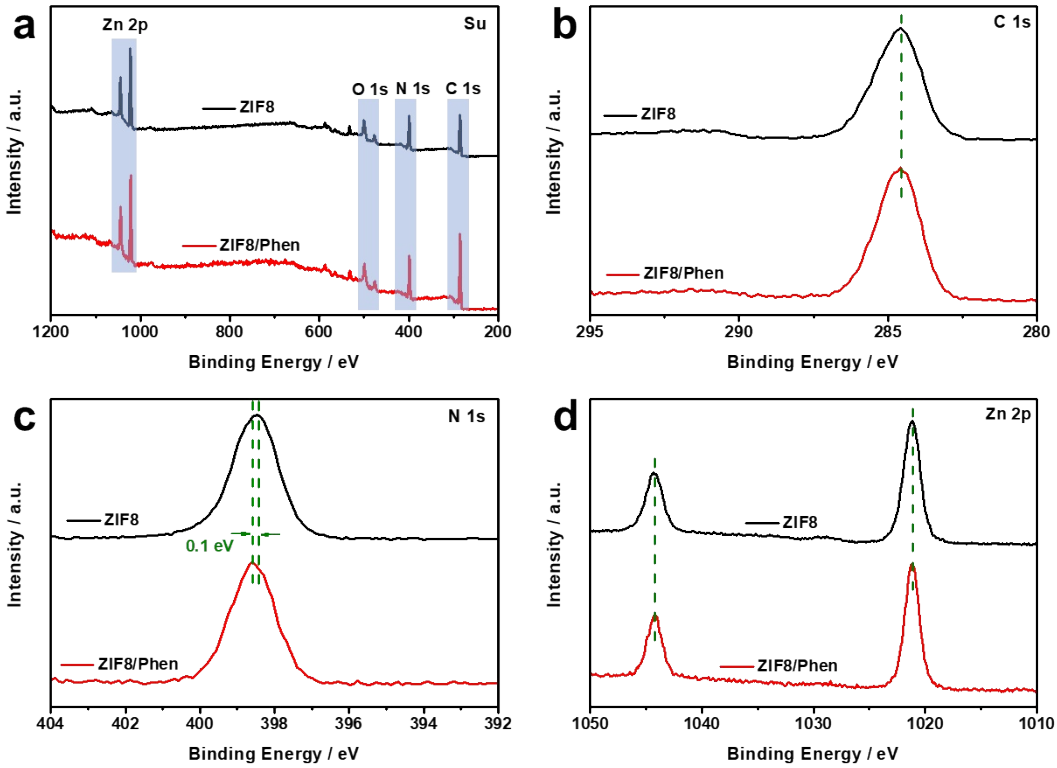

Fig. S4 XPS spectra of ZIF8 and ZIF8/Phen precursors. (a) survey spectra; (b) C 1s spectra; (c) N1s spectra; (d) Zn 2p spectra.

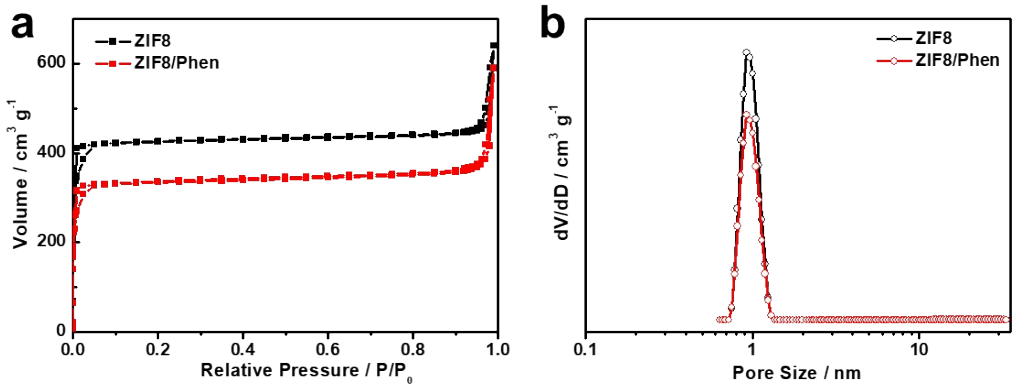

Fig. S5 N_2 adsorption-desorption isotherms (a) and the corresponding pore size distribution curves of the ZIF8 and ZIF8/Phen precursors (b).

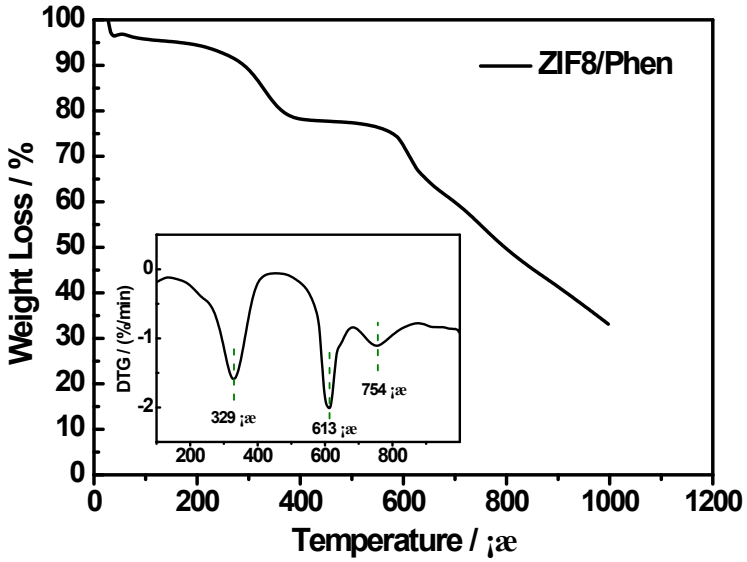

Fig. S6 TG curve of the ZIF8/Phen under nitrogen with a heating rate of 10 °C min^{-1}. The decomposition temperature of ZIF8 is ~886 K.

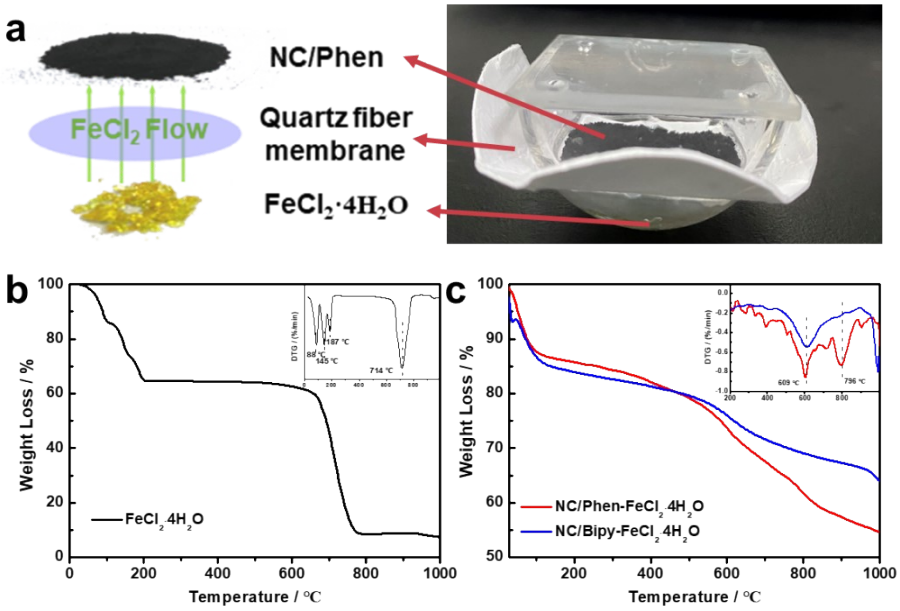

Fig. S7 (a) The device of the bottom-up "$FeCl_2$ steam capture" strategy. TG curve of the $FeCl_2 \cdot 4H_2O$ (b), NC/Phen-$FeCl_2 \cdot 4H_2O$ and NC/Bipy-$FeCl_2 \cdot 4H_2O$ (c) under nitrogen with a heating rate of 10 K min^{-1}.

Thermogravimetric analysis (TGA) of $FeCl_2 \cdot 4H_20$ showed that $FeCl_2$ molecule is vapored at about 987 K. Thus, $FeCl_2$ can be transported by gas phase at 1023 K and be seized by the surface-rich pyridinic-N carbon shell, further formation of Fe-N_4 sites.

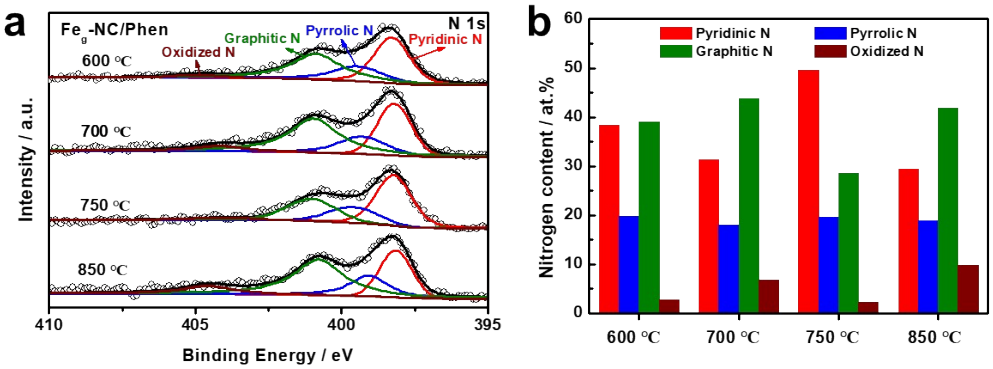

Fig. S8 XPS N 1s spectra (a) and the corresponding N species relative content (b) of Fe$_g$-NC/Phen with different pyrolysis temperature. The pyridinic N content was highest at 1023 K, indicating the possible highest ORR activity.

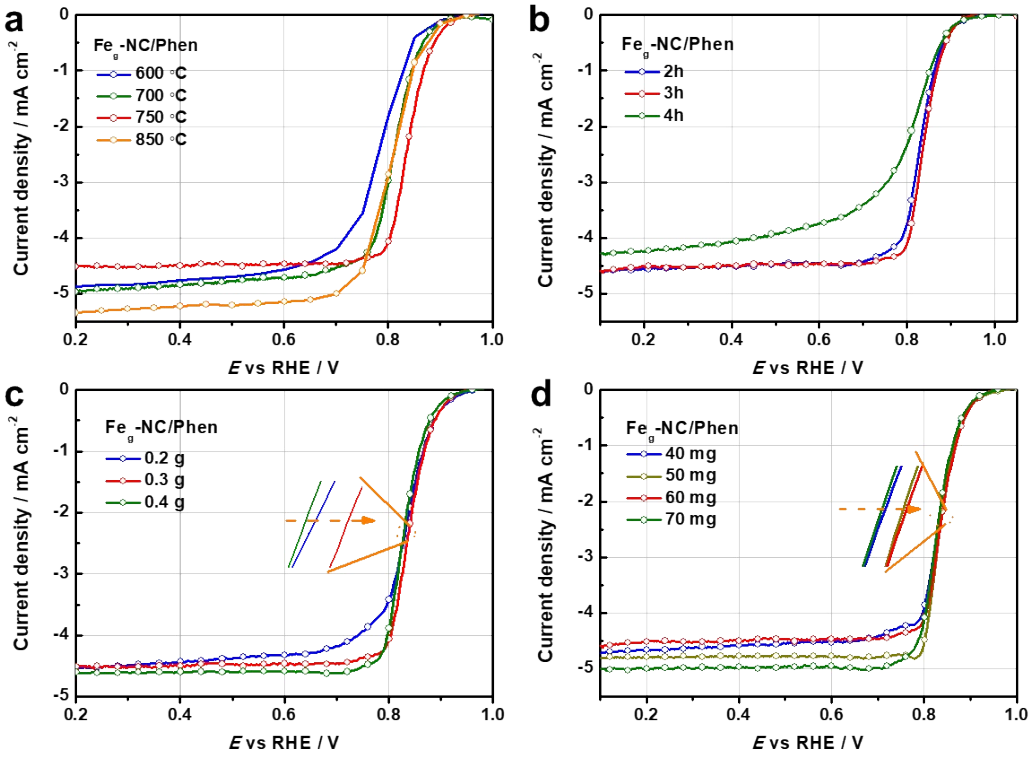

Fig. S9 ORR polarization curves of Fe_g-NC/Phen samples under different synthetic conditions. (a) pyrolysis temperature; (b) pyrolysis time; (c) mass of Phen; (d) mass of $FeCl_2 \cdot 4H_2O$. Test conditions: O_2-saturated 0.1 M H_2SO_4, 900 rpm, sweep rate of 10 mV s^{-1} and catalyst loading of 0.6 mg cm^{-2} for Fe-N-C catalysts, graphite rod as counter electrode.

The performance of Fe_g-NC/Phen reached the highest at 1023 K for 3h. And the optimized doping amount of Phen and $FeCl_2 \cdot 4H_2O$ are 0.3 g and 60 mg.

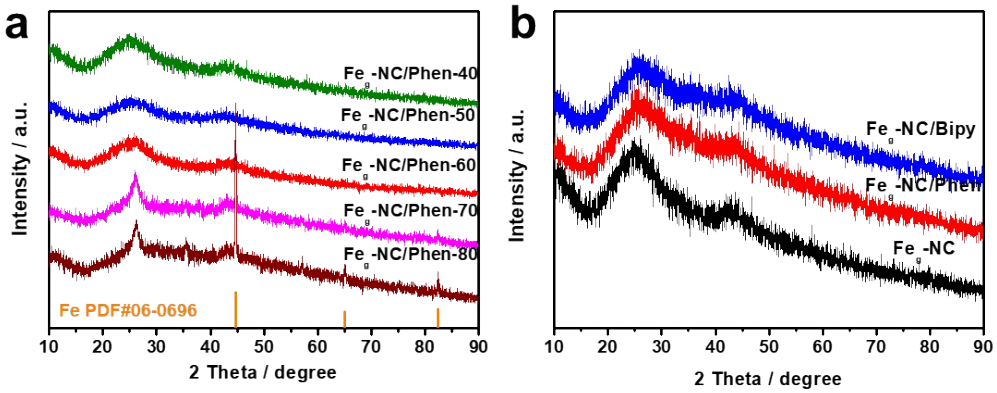

Fig. S10 XRD patterns of the (a) Fe_g-NC/Phen with different mass of iron; (b) Fe_g-NC, Fe_g-NC/Phen and Fe_g-NC/Bipy samples.

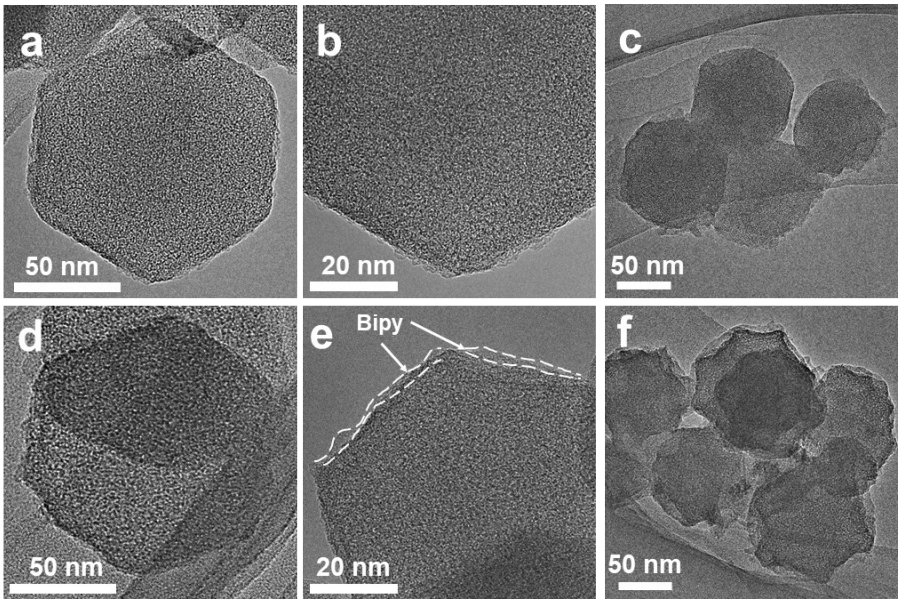

Fig. S11 TEM images of the NC (a-b), Fe_g-NC (c), NC/Bipy (d-e) and Fe_g-NC/Bipy (f).

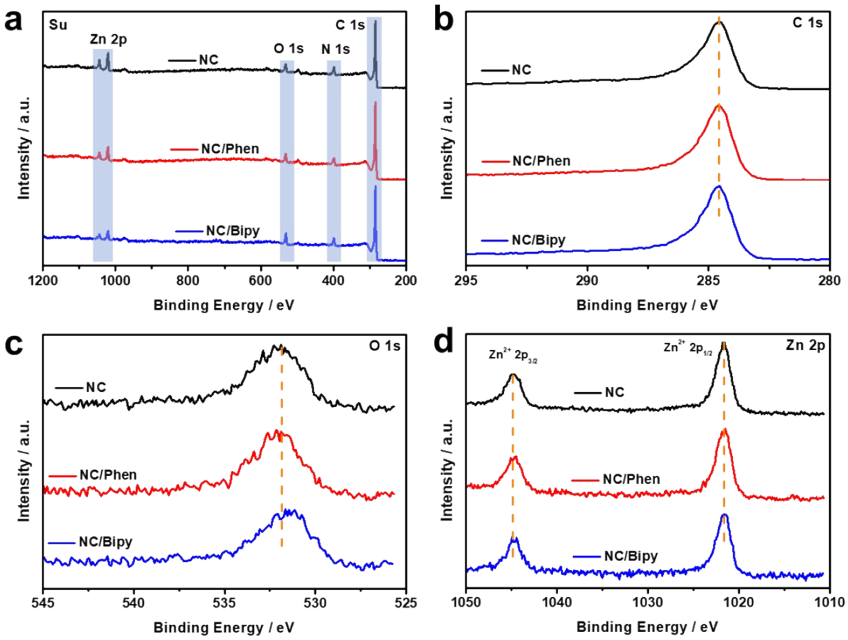

Fig. S12 XPS analysis of the NC, NC/Phen and NC/Bipy samples. (a) survey spectra; (b) C 1s spectra; (c) O 1s spectra; (d) Zn 2p spectra.

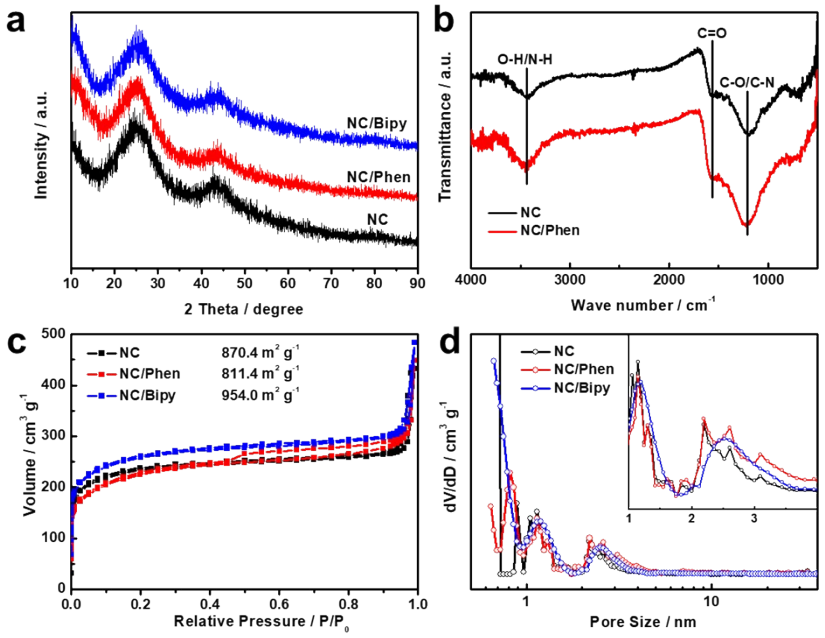

Fig. S13 (a) XRD patterns of the NC, NC/Phen and NC/Bipy samples. (b) FTIR spectra of NC and NC/phen samples. N_2 adsorption-desorption isotherms (c) and the corresponding pore size distribution curves (d) of the NC, NC/Phen and NC/Bipy samples.

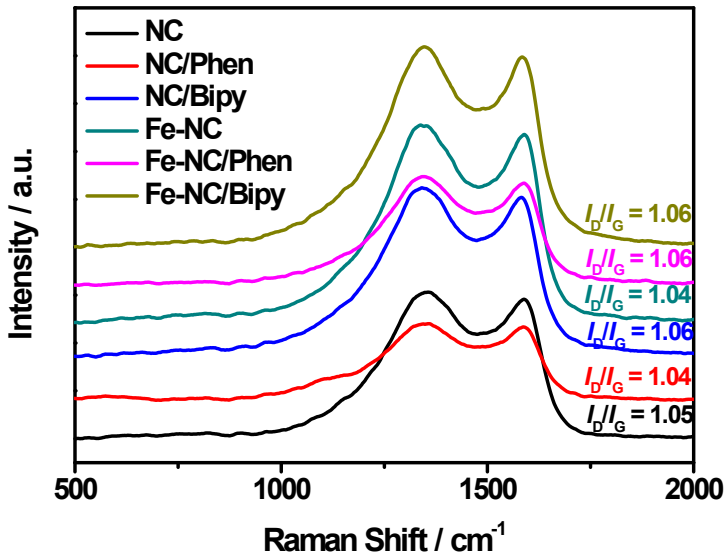

Fig. S14 Raman spectra of different samples.

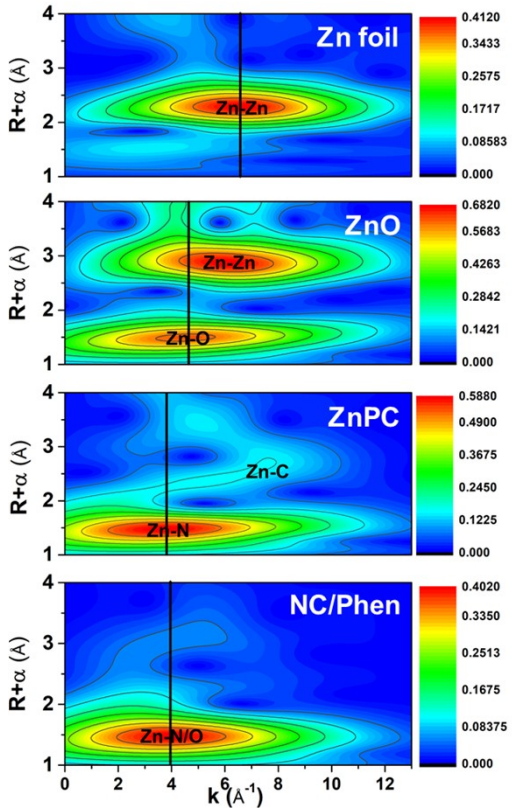

Fig. S15 Zn K-edge WT-EXAFS contour plots of NC/Phen.

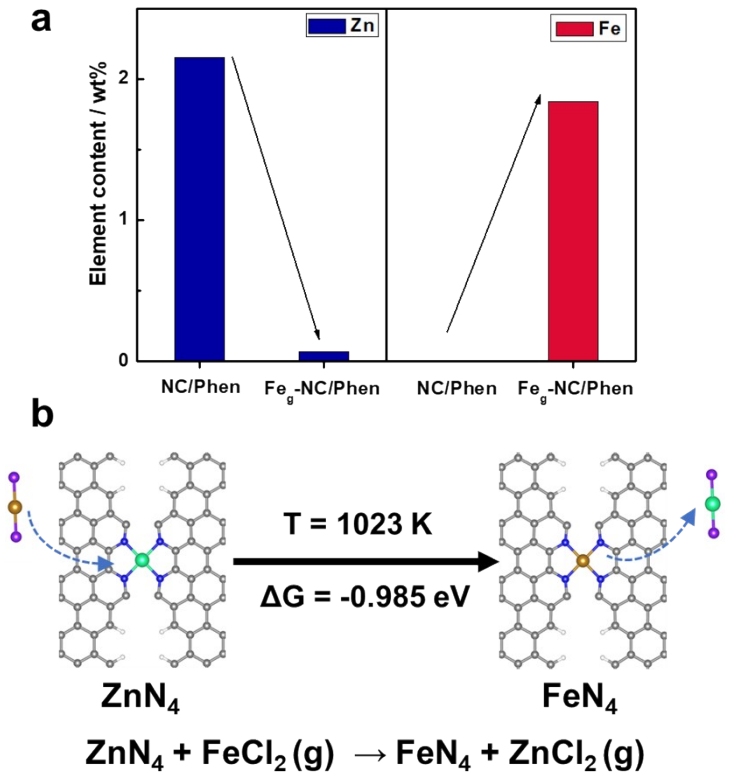

Fig. S16 (a) Element content before and after seizing gaseous $FeCl_2$. (b) Computational prediction of transformation of ZnN_4 to FeN_4 sites under 1023 K. The green, brown, blue and grey balls represent Zn, Fe, N and C atoms, respectively.

Jiao *et al*[1] discussed the site mechanism by temperature-programmed reaction (TPR) and online ICP-MS and proposed that Fe-N_4 sites are formed via high-temperature trans-metalation that involves the exchange of Fe and Zn between Zn-N_4 and $FeCl_3$:

$FeCl_3$ + Zn-N_4 + X ⟶ Fe-N_4 + $ZnCl_2$ (g) + XCl

In fact, the trans-metalation mechanism was proposed by Fellinger *et al*[2, 3] to account for the exchange of Fe and Zn between Zn-N_4 and Fe-N_4. Based on the work of these literatures, we found that the decrease in surface Zn content was accompanied by an increase in surface Fe content, suggesting the exchange of Fe and Zn between Zn–N_4 and gaseous Fe^{2+}. Besides, DFT calculations show that it is thermodynamically favorable for conversion of ZnN_4 to FeN_4 at 1023 K. Thus, we proposed the transformation mechanism:

ZnN_4 + $FeCl_2$ (g) ⟶ FeN_4 + $ZnCl_2$ (g)

References

1. L. Jiao, J. Li, L. L. Richard, Q. Sun, T. Stracensky, E. Liu, M. T. Sougrati, Z. Zhao, F. Yang, S. Zhong, H. Xu, S. Mukerjee, Y. Huang, D. A. Cullen, J. H. Park, M. Ferrandon, D. J. Myers, F. Jaouen and Q. Jia, *Nat. Mater.*, 2021, 20, 1385-1391.
2 A. Mehmood, J. Pampel, G. Ali, H. Y. Ha, F. Ruiz-Zepeda and T.-P. Fellinger, *Adv. Energy Mater.*, 2018, **8**, 1701771.
3 D. Menga, F. Ruiz-Zepeda, L. Moriau, M. Šala, F. Wagner, B. Koyutürk, M. Bele, U. Petek, N. Hodnik, M. Gaberšček and T. P. Fellinger, *Adv. Energy Mater.*, 2019, **9**, 1902412.

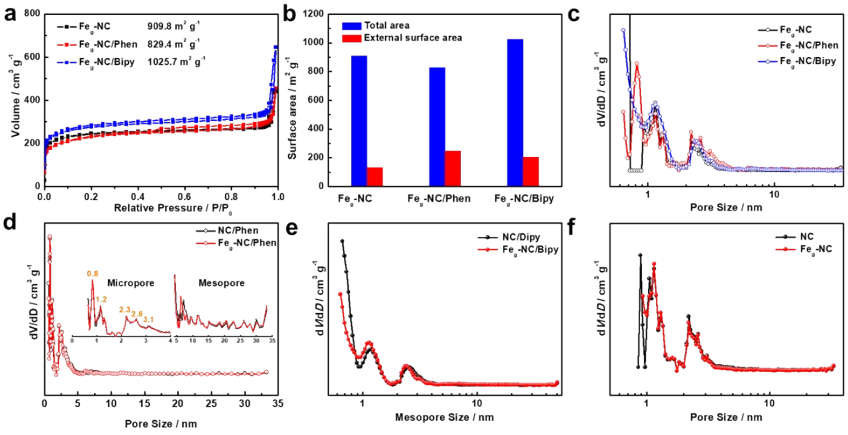

Fig. S17 N_2 adsorption-desorption isotherms (a) and the corresponding external surface area (b) of the Fe_g-NC, Fe_g-NC/Phen and Fe_g-NC/Bipy samples. (c-f) The pore size distribution curves of the Fe_g-NC, Fe_g-NC/Phen and Fe_g-NC/Bipy samples.

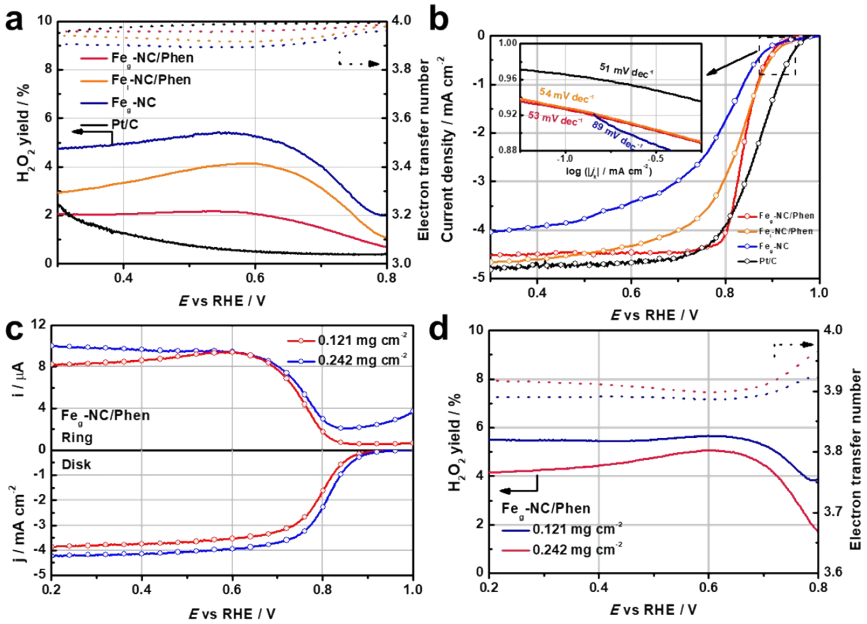

Fig. S18 (a) Number of transferred electrons and yield of H_2O_2; (b) Tafel plots curves of Fe_g-NC/Phen, Fe_I-NC/Phen, Fe_g-NC and Pt/C; (c) The RRDE polarization curves of Fe_g-NC/Phen; (d) peroxide yield. Catalyst loading is 0.121 mg cm^{-2} and 0.242 mg cm^{-2}.

The efficiency of the ORR process on Fe/N-C was evaluated by using a rotating ring−disk electrode (RRDE) experiment and Koutecky−Levich plots. The electron transfer number of Fe_g-NC/Phen is about 3.9, and its peroxide yield is below 6%. The peroxide yield was almost certainly an "apparent" value, the result of a 2+2 ORR mechanism occurring in the very thick layer of Fe_g-NC/Phen. A true peroxide yield should have been determined at much lower catalyst disk loadings than 0.3 mg cm^{-2}. Thus, the catalyst disk loading was reduced to 0.1 mg cm^{-2}, and the peroxide yield was still below 6%, suggesting that the it was favour for 4-electron reduction mechanism for ORR.

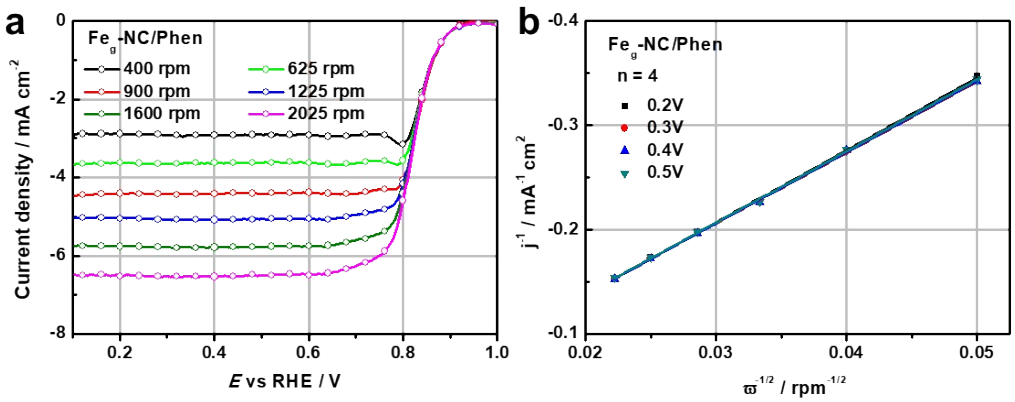

Fig. S19 (a) ORR polarization curves of Fe_g-NC/Phen at different rotating rates in 0.1 M H_2SO_4; (b) The corresponding K-L plots of Fe_g-NC/Phen.

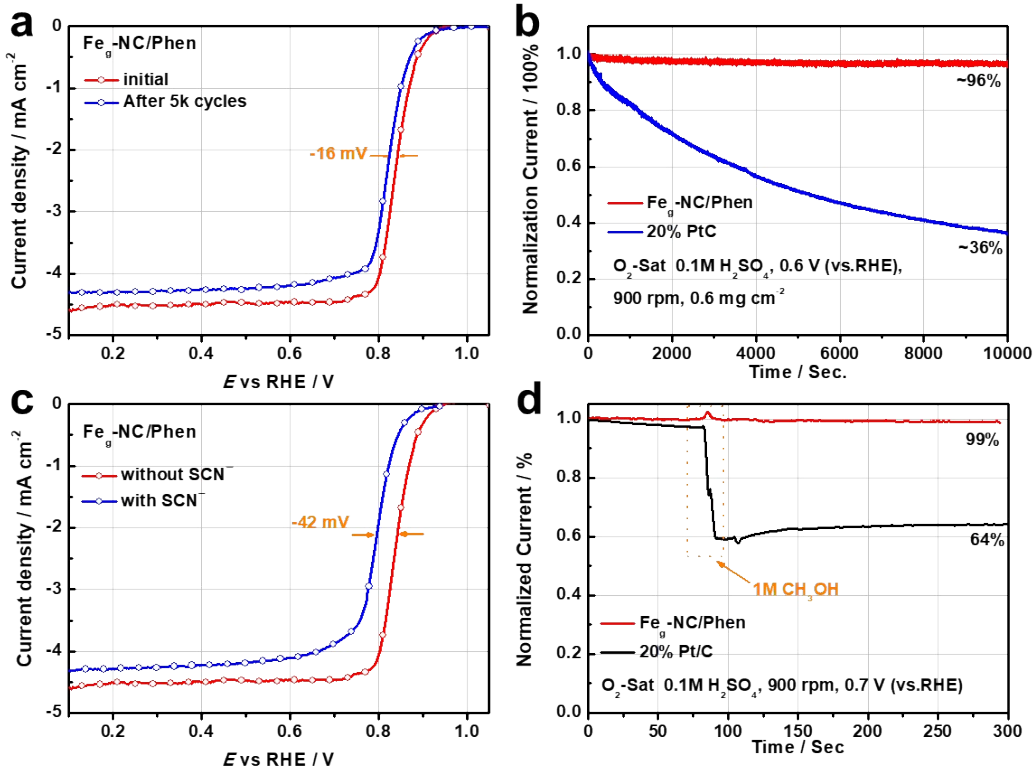

Fig. S20 (a) ORR polarization curves before and after 5000 cycles between 0.6 and 1.0 V *vs* RHE in 0.1 M H_2SO_4; (b) Chronoamperometric responses of Fe_g-NC/Phen and 20% Pt/C at 0.6 V *vs* RHE; (c) ORR polarization curves with or without SCN^-; (d) Chronoamperometric responses of Fe_g-NC/Phen and 20% Pt/C samples in 0.1 M H_2SO_4 before and after addition of 1 M methanol.

The stability of Fe_g-NC/Phen was assessed by the accelerated degradation test (ADT) in acidic media. The $E_{1/2}$ was negative shift 16 mV after 5000 cycles, which was similar to Fe-N-C catalysts reported previously. The data of chronoamperometry showed that Fe_g-NC/Phen possessed the good stability in RDE test environment. We used SCN^- to prove that Fe was the active sites due to the strong adsorptuon between SCN^- and Fe^{2+}, the $E_{1/2}$ was negative shift 42 mV after SCN^- poisoned, indicating that Fe was the main active sites. We have measured the tolerance to methanol of Fe_g-NC/Phen compared with Pt/C electrocatalyst. It revealed only slight decrease of Fe_g-NC/Phen after the addition of methanol compared with Pt/C electrocatalyst, indicating very good tolerance to methanol of Fe_g-NC/Phen.

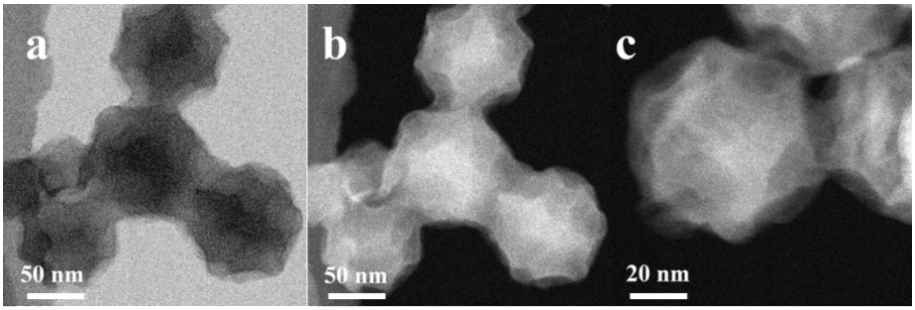

Fig. S21 (a) TEM, (b,c) HAADF STEM images of Fe_g-NC/Phen after stability tests. The morphology of Fe_g-NC/Phen were still stable after stability tests.

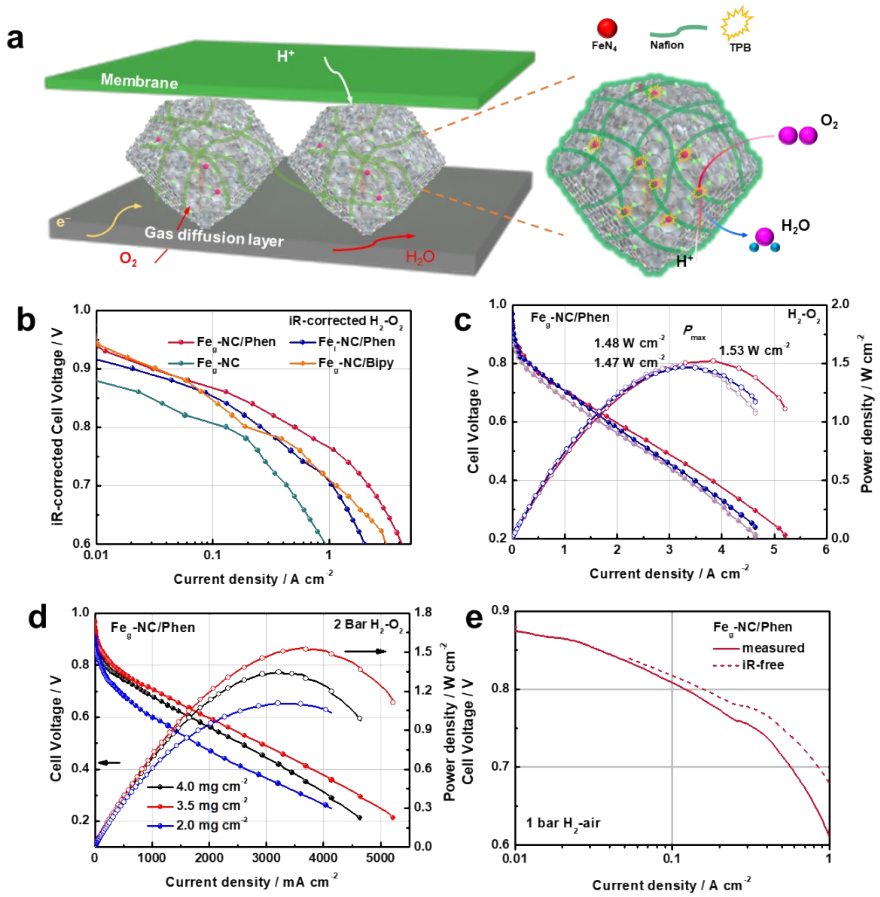

Fig. S22 (a) A schematic illustration of TPB active sites in the Fe_g-NC/Phen catalyst-based electrodes. (b) Tafel plots of the iR-free polarization curves for MEAs in **Fig. 4**a. (c) Repeated measurements of fuel cells. (d) Polarization and power density curves of the Fe_g-NC/Phen prepared with different cathode loading. (e) Tafel plots of the iR-free polarization curves for MEAs in **Fig. 4**d . Test conditions: anode loading 0.4 mg_{Pt} cm^{-2}, Nafion 211 membrane, 4.41 cm^2 electrode area, 353 K, 100%RH, 2.0 bar H_2-O_2.

It was found that 3.5 mg cm^{-2} was the best loading by PEMFCs polariation curves under different catalyst loading. Besides, good repeatability of the high power performance was shown through repeated experiments.

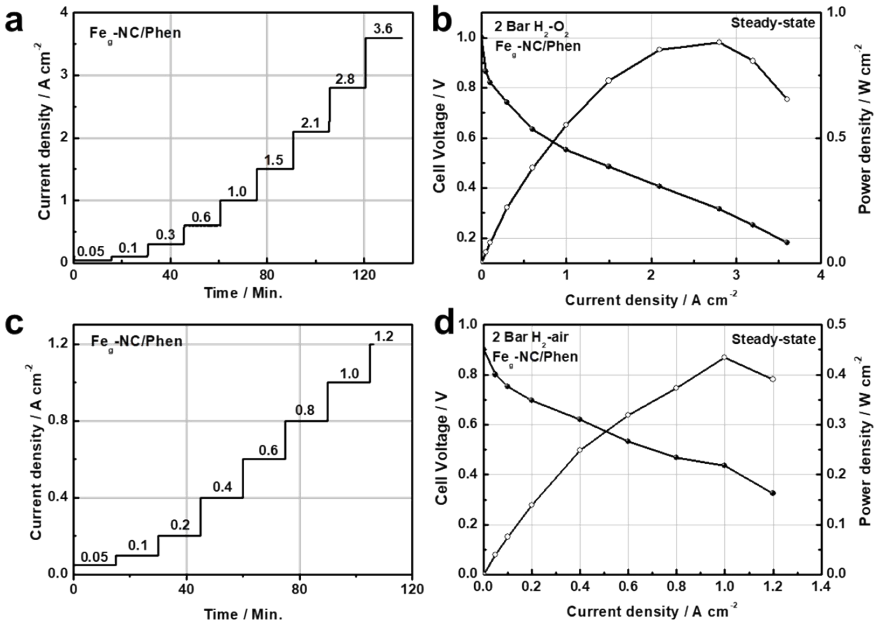

Fig. S23 (a, c) Test condition and steady-state polarization curves and power density curves of the Fe_g-NC/Phen in 2.0 bar H_2-O_2 (b) and in 2.0 bar H_2-air (d), respectively.

We further evaluated the practical applicability of Fe_g-NC/Phen by steady state testing. Fe_g-NC/Phen still displayed 0.9 W cm^{-2} and 0.44 W cm^{-2} in 2 bar H_2–O_2 and H_2–air, respectively, indicating that Fe_g-NC/Phen still showed practical performance under working conditions.

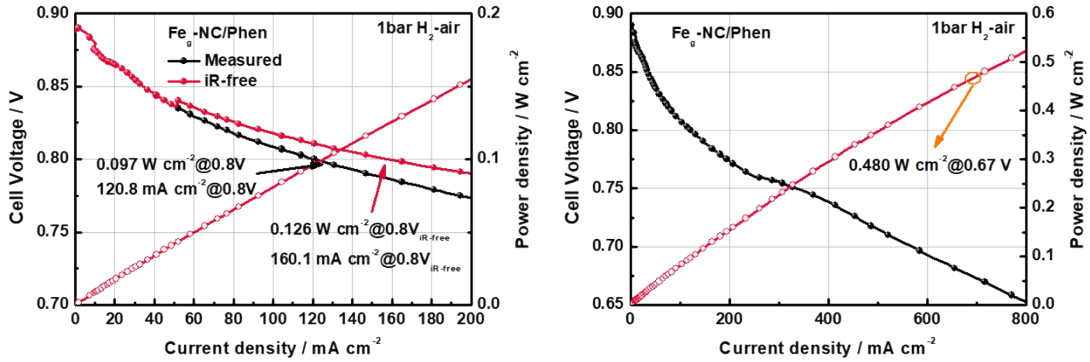

Fig. S24 The MEAs air performance at 0.8 V and 0.67 V of Feg-NC/Phen at 80 ^{o}C.

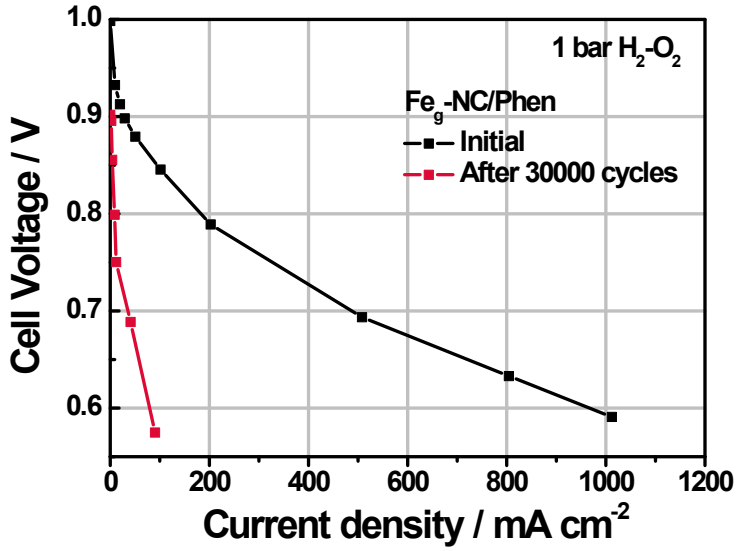

Fig. S25 Fuel cell polarization curves of Fe_g-NC/Phen before and after 30,000 voltage cycling.

The MEAs durability is determined by multiple factors, and the production process of MEAs is complex, including coating, hot pressing and assembly. Besides, other environmental factor such as temperature, humidity, hydrophilic and hydrophobic may influence the durability of MEAs. The durability is a serious issue for the application of PGM-free catalyst in fuel cell. It is difficult to balance the activity and durability in the study of PGM-free catalyst. Thus, there is an urgent need to improve the stability of Fe-N-C catalysts.

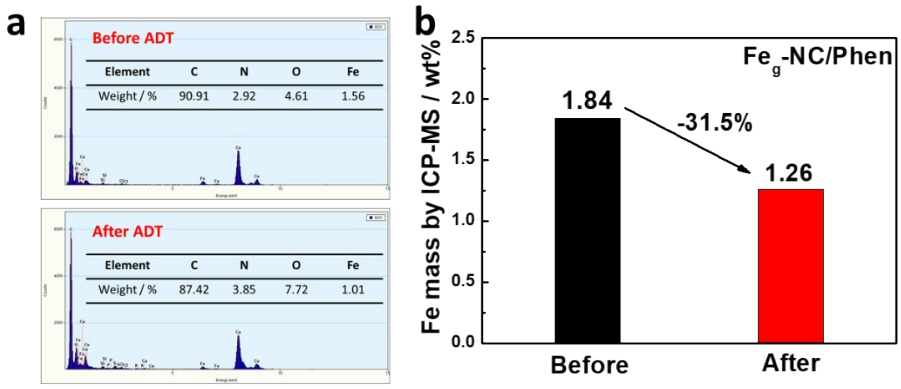

Fig. S26 EDX and ICP-MS analysis of Fe_g-NC/Phen before and after 10000 cycles between 0.6 and 1.0 V vs RHE in 0.1 M H_2SO_4.

We have calculated the Fe dissolution percentage of Fe_g-NC/Phen after 10000 cycles stability test. We can find that Fe mass decreases after 10000 cycles stability test by EDX and ICP-MS. Then the Fe dissolution percentage of Fe_g-NC/Phen is about 31.5%, indicating the unstable surface Fe-N_4 moieties, consistent with the poor durability in PEMFCs.

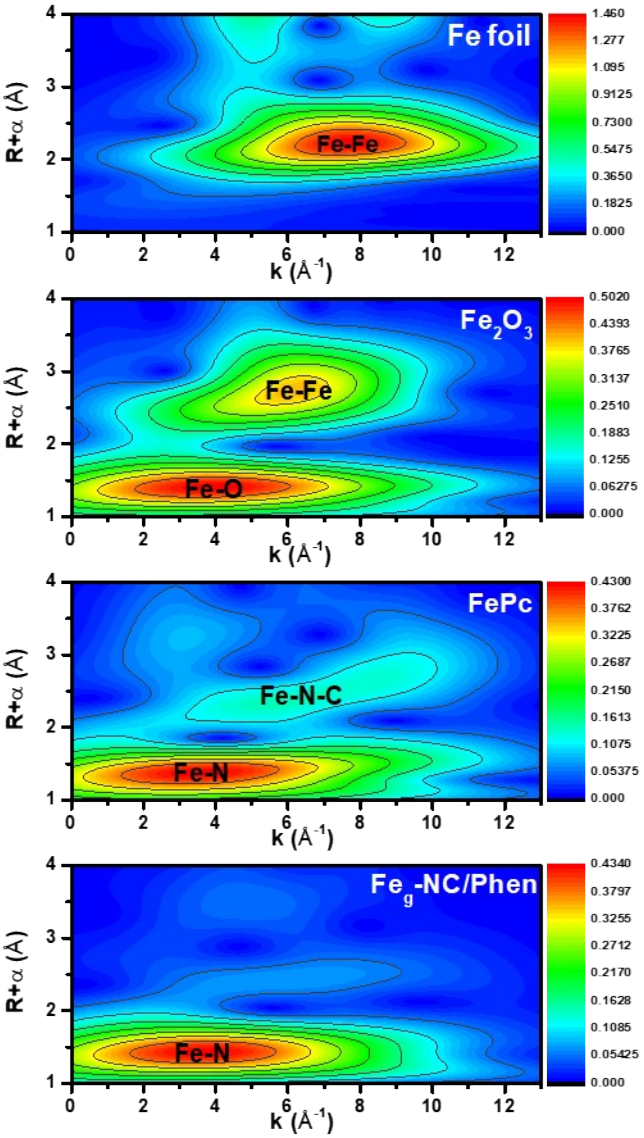

Fig. S27 Fe K-edge WT-EXAFS contour plots of Fe_g-NC/Phen.

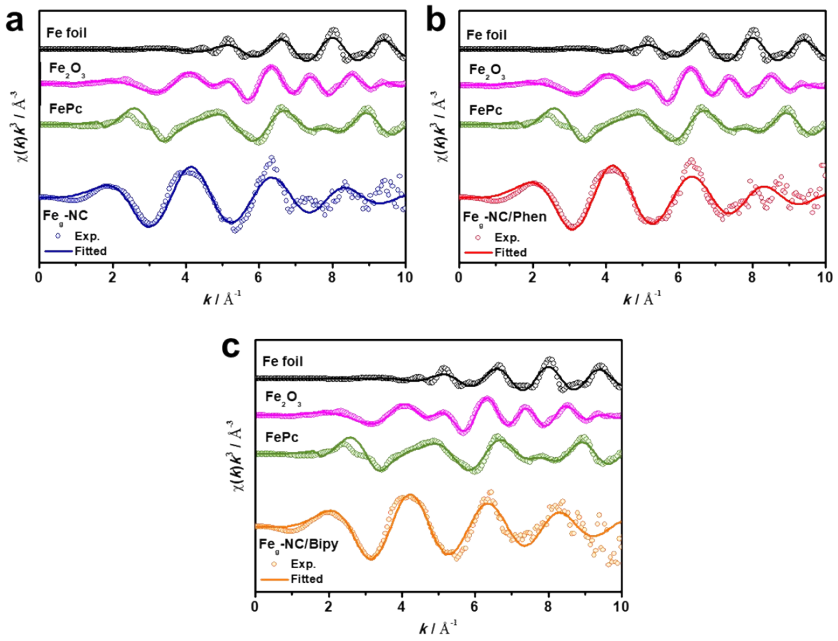

Fig. S28 EXAFS fitting of Fe_g-NC, Fe_g-NC/Phen and Fe_g-NC/Bipy in *k* space.

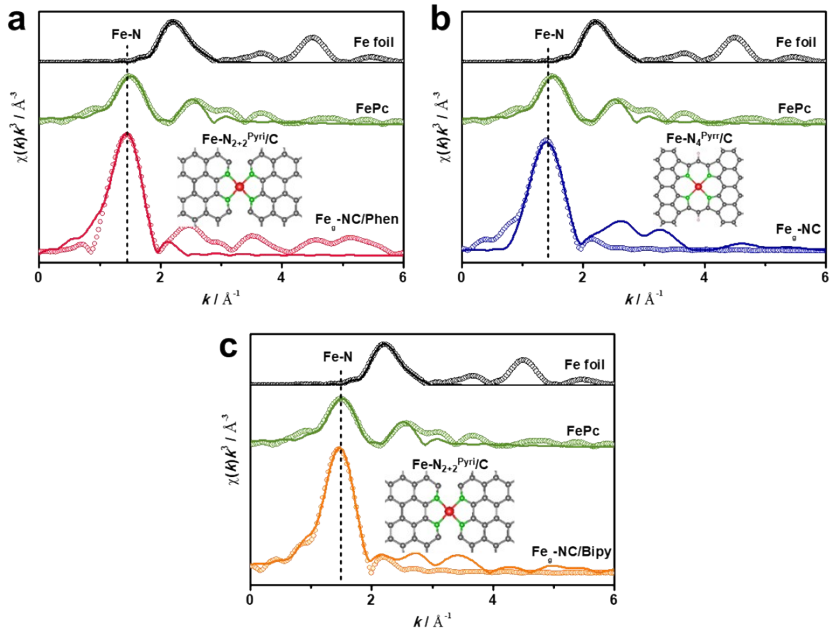

Fig. S29 EXAFS fitting of Fe_g-NC, Fe_g-NC/Phen and Fe_g-NC/Bipy in *R* space.

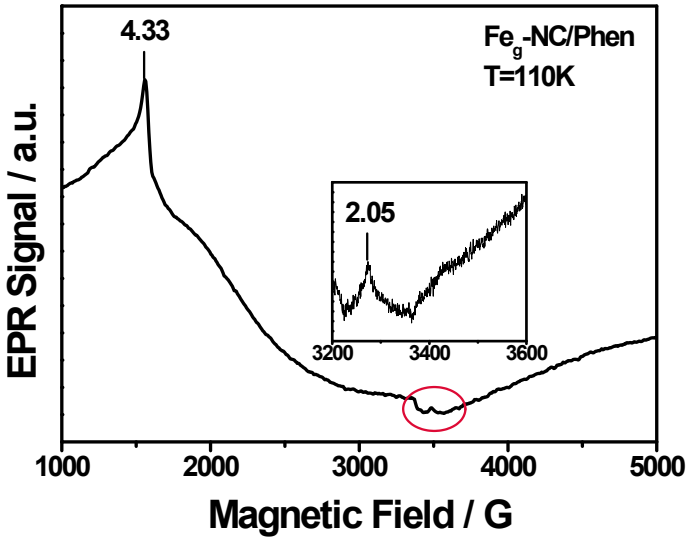

Fig. S30 EPR spectra of Fe_g-NC/Phen at 110 K. The *g* values are indicated in the figure.

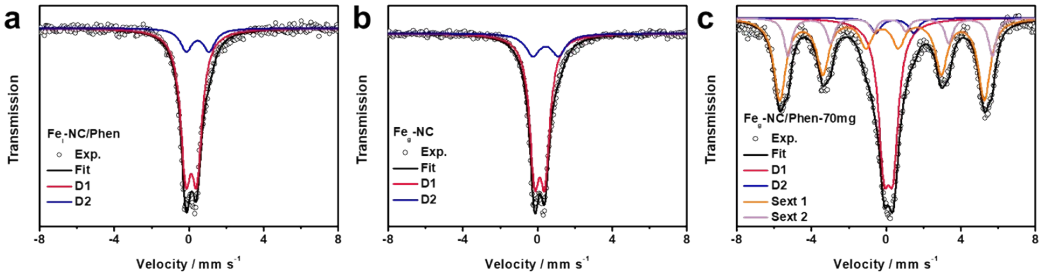

Fig. S31 The ^{57}Fe Mössbauer spectrum measured at 298 K. Exp., experiment of (a) Fe_I-NC/Phen, (b) Fe_g-NC and (c) Fe_g-NC/Phen-70mg.

The absolute value of the quadrupole splitting (ΔE_Q) for D1 site is about 0.55 mm s^{-1} (Table S10), corresponding to the Fe(III) (S=5/2) or Fe(II) (S=0).[1] While D1 site was only assigned as low spin Fe-N_4 without specifications of possible additional ligands. One nitrogen/oxygen ligand (possibly connected to an underlying graphene layer) and an oxygen molecule as sixth ligand. As these Fe–N–C catalysts reveal a high affinity towards oxygen, it is natural that they might form related coordination upon contact with air.[2] According to previous literatures, Fe-N-C catalysts were easy to adsorb reversibly one or two axial O_2 at the Fe centers.[3-5] Thus, we think D1 site should be assigned as O_2-Fe(III)-N_4 site, which Fe is expected to be binding O_2 and forming Fe(III)-N_4 sites upon contact with air.

The $FeCl_2{\cdot}4H_2O$ mass of Fe_g-NPs-NC/Phen was 70 mg, which was only 10 mg higher than that of Fe_g-NC/Phen. The typical sextet corresponded to iron species was detected as increased 10 mg of $FeCl_2{\cdot}4H_2O$, suggesting the bottom-up "$FeCl_2$ steam capture" strategy could easily introduce iron into NC/Phen (**Table S**7).

References

1. C. Gallenkamp, U. I. Kramm, J. Proppe and V. Krewald, Int. J. of Quantum Chem., 2020, 121.
2. U. I. Kramm, L. Ni and S. Wagner, Adv. Mater., 2019, 31, e1805623.
3. X. Wan, X. Liu, Y. Li, R. Yu, L. Zheng, W. Yan, H. Wang, M. Xu and J. Shui, Nat. Catal., 2019, 2, 259-268.
4. A. Zitolo, V. Goellner, V. Armel, M. T. Sougrati, T. Mineva, L. Stievano, E. Fonda and F. Jaouen, Nat. Mater., 2015, 14, 937-942.
5. X. Zhang, X. Han, Z. Jiang, J. Xu, L. Chen, Y. Xue, A. Nie, Z. Xie, Q. Kuang and L. Zheng, Nano Energy, 2020, 71, 104547.

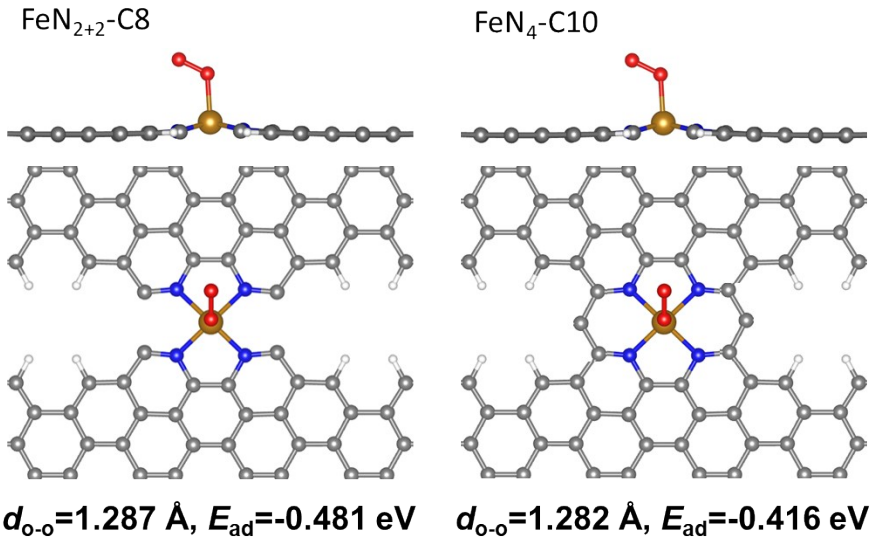

Fig. S32 The O-O bond lengths and O_2 adsorption energy calculated at different optimized model structures.

At the FeN_4-C10 structure, the FeN_4 moiety is embedded into hexagonal carbon layer and surrounded by 10 carbon atoms. It can be applied to simulate the conventional FeN_4 moiety in the catalyst. At the FeN_{2+2}-C8 structure, there are a pair of pores near both sides of FeN_4 moiety, so that the Fe center can be considered to bridge the two adjacent edges of N coordinated graphene rings. This edge structure is quite similar to the local N-heterocyclic rings of Phenanthroline (Phen). Therefore, this structure can be used to simulate the active site that can be obtained in our proposed synthesis method. As regards the FeN_4-C10 structure, the O_2 adsorption at the Fe center dominates in the end-on configuration, in which the Fe center is in the low-spin state. The adsorption energy is -0.416 eV, and the corresponding O-O and Fe-O bond lengths are 1.282 Å. By comparison, the same adsorption configuration is investigated at the FeN_{2+2}-C8 structure. The adsorption energy is -0.481 eV, and the relevant O-O bond length is 1.287 Å, respectively. Therefore, O_2 adsorption in the end-on configuration is activated to a small degree at the FeN_{2+2}-C8 structure compared with the FeN_4-C10 structure. This can be ascribed to the change in the electronic structure of Fe center, because of the difference in the local coordination structure around the Fe center. The Fe-N bond in the FeN_{2+2}-C8 structure on average is relatively long than that in the FeN_4-C10, as revealed experimentally, indicating a slightly weaker Fe-N interaction at

the FeN_{2+2}-C8 than the FeN_4-C10. Consequently, O_2 can interact with the Fe center of FeN_{2+2}-C8 relatively strongly rather than the FeN_4-C10. The Fe-O bond length in the FeN_{2+2}-C8 is found to be 1.979 Å, which is relatively shorter than that in the FeN_4-C10 (1.997 Å) (**Table S11**). This leads to the activation of O_2 adsorption at those structures to different extents. Therefore, our synthesis strategy not only can maximize the active site density at the external layers of the catalyst, but also can adjust the electronic structure of Fe center to enhance ORR activity.

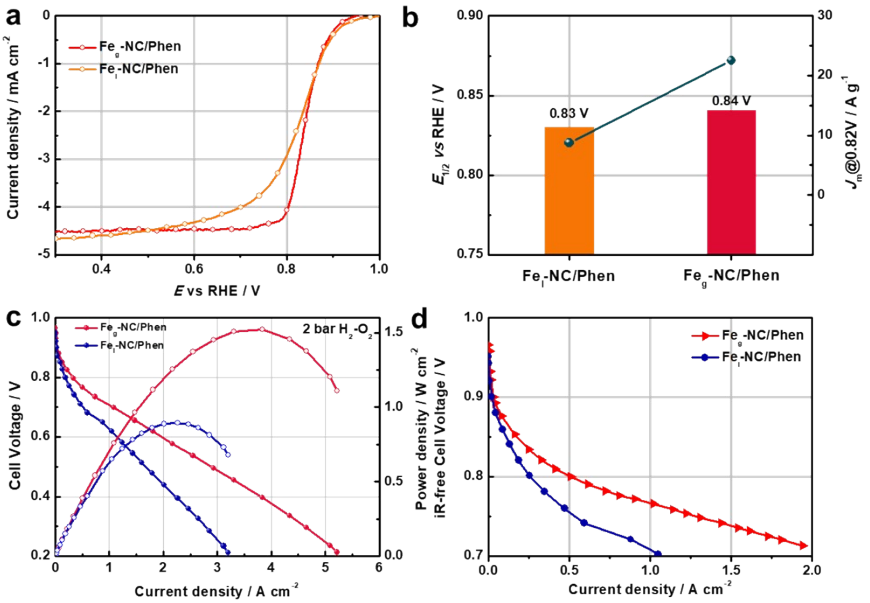

Fig. S33 (a) ORR polarization curves; (b) $E_{1/2}$ and J_m at 0.82 V; (c) H_2-O_2 PEMFC polarization and power density curves. Cathode, 3.5 mg_{cat} cm^{-2} for Fe-N-C; anode, 0.4 mg_{Pt} cm^{-2}; Nafion 211 membrane; 4.41 cm^2 electrode; 353 K, 100% relative humidity (RH); 400 mL O_2 min^{-1} and 300 mL H_2 min^{-1}. (d) Polarization curves with iR-free.

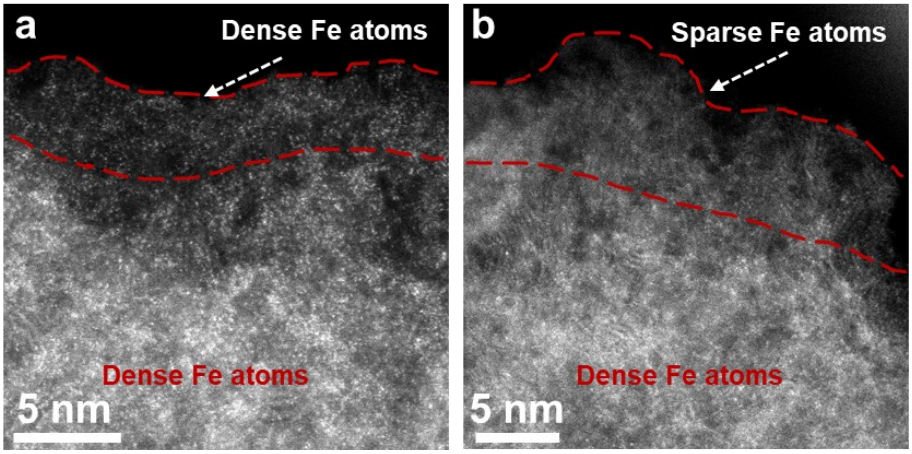

Fig. S34 AC HAADF-STEM images of (a) Fe_g-NC/Phen and (b) Fe_I-NC/Phen.

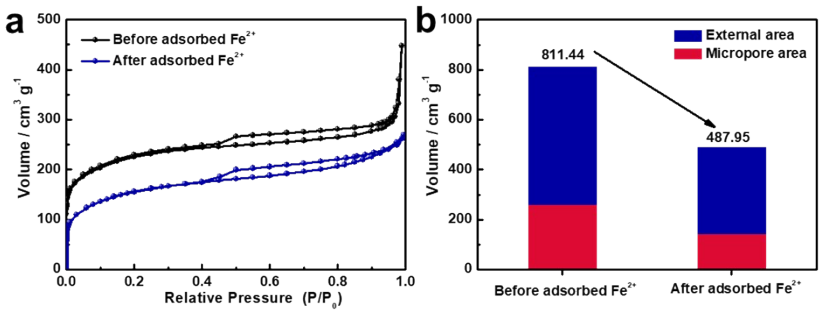

Fig. S35 N_2 adsorption-desorption isotherms (a) and the corresponding external surface area (b) of the Fe_I-NC/Phen.

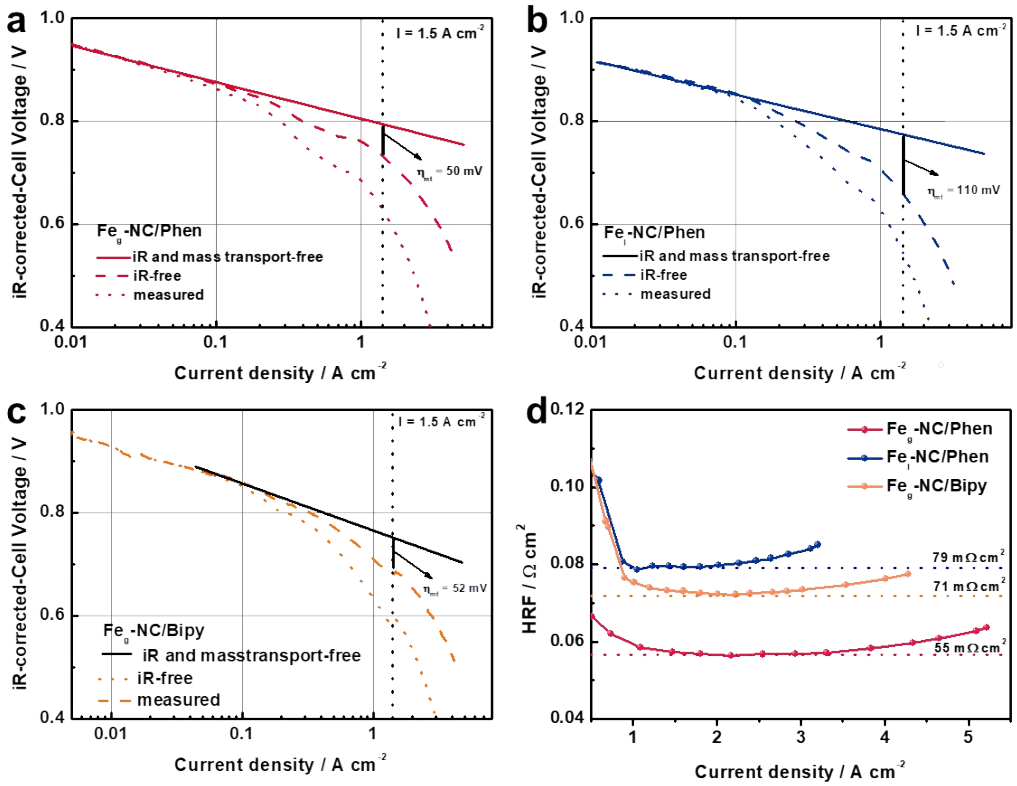

Fig. S36 Determination of the mass-transport overpotential (η_{mt}) of Fe_g-NC/Phen, Fe_l-NC/Phen and Fe_g-NC/Bipy. Tafel plots of the PEMFC iR-free polarization curves (short dot lines) and measured polarization curves (short dash lines) of the catalysts (a) Fe_g-NC/Phen, (b) Fe_l-NC/Phen and (c) Fe_g-NC/Bipy. (d) HRF of Fe_g-NC/Phen, Fe_l-NC/Phen and Fe_g-NC/Bipy. The conceptual polarization curves (solid line) in the absence of mass transport and ohmic resistances can be constructed by extrapolating the iR-free cell voltage obtained at low current densities. The difference between the conceptual polarization curve and the iR-free polarization at a certain current density can be determined as the mass-transport overpotential (η_{mt}).

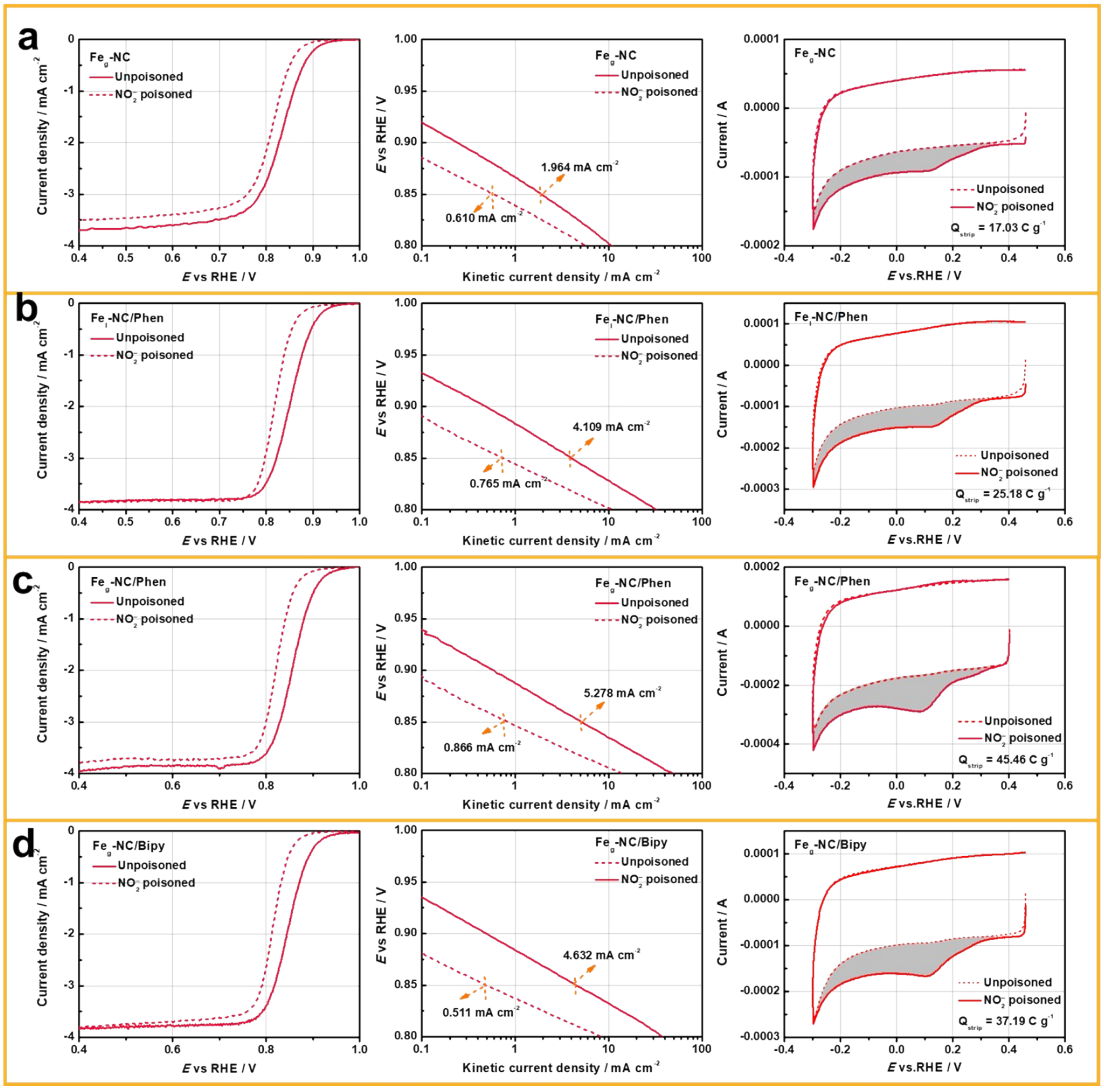

Fig. S37 Determination of SD of (a) Fe_g-NC, (b) Fe_I-NC/Phen, (c) Fe_g-NC/Phen and (d) Fe_g-NC/Bipy samples. Left column, LSV curves before and after nitrite adsorption in a 0.5 M acetate buffer at pH 5.2. Middle column, kinetic current density before and after nitrite adsorption. Right column, CV curves before and during nitrite adsorption in the nitrite reductive stripping region. Catalyst loading is 0.242 mg cm^{-2}.

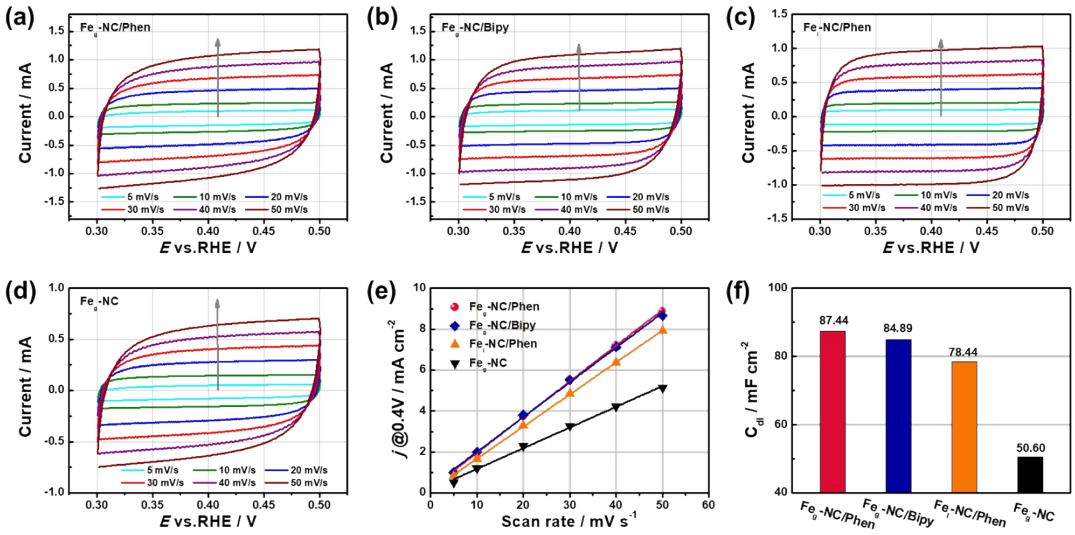

Fig. S38 CV curves of (a) Fe_g-NC/Phen, (b) Fe_g-NC/Bipy, (c) Fe_I-NC/Phen and (d) Fe_g-NC in N_2 saturated 0.1 M H_2SO_4, (e) fitting plots of the current density at 0.40 V versus the scan rates to determine the C_{dl}, (f) corresponding C_{dl} of catalysts.

Electrochemically active surface area (ECSA) is also an important factor to provide more information on the active sites of the catalysts. The assessment of ECSA through double layer capacitances (C_{dl}) based on CV measurements at different scan rates. The C_{dl} was determined by measuring the capacitive current associated with double-layer charging from the scan-rate dependence of cyclic voltammetric curves. For this, the potential window of cyclic voltammetric stripping was 0.3 V to 0.5 V versus RHE (non-faradaic region). The scan rates were 5 mV s^{-1}, 10 mV s^{-1}, 20 mV s^{-1}, 30 mV s^{-1}, 40 mV s^{-1}, 50 mV s^{-1}. The C_{dl} was estimated by plotting the $\Delta j = (j_a - j_c)$ at 0.40 V (where j_c and j_a are the cathodic and anodic current densities, respectively) versus RHE against the scan rate, in which the slope was twice that of C_{dl}. It evidenced that Fe_g-NC/Phen possessed a C_{dl} value of 87.44 mF cm^{-2}, closed to Fe_g-NC/Bipy (84.89 mF cm^{-2}) and Fe_I-NC/Phen (78.44 mF cm^{-2}), superior to Fe_g-NC (50.60 mF cm^{-2}), indicating that the modification of pyridinic-N-like organic ligands could improve the ECSA and ORR performance.

Table S1. Porosity of ZIF8, ZIF8/Phen, NC, NC/Phen, NC/Bipy, Fe_g-NC, Fe_g-NC/Phen and Fe_g-NC/Bipy materials.

Samples	S_{BET} / m^2 g^{-1}	S_{Micro} / m^2 g^{-1}	S_{Meso} / m^2 g^{-1}	Pore Volume / m^3 g^{-1}
ZIF8	1788.7	1733.0	55.7	0.428
ZIF8/Phen	1399.1	1338.0	61.1	0.337
NC	870.4	725.0	145.4	0.240
NC/Phen	811.4	551.3	260.1	0.237
NC/Bipy	954.0	744.5	209.5	0.268
Fe_g-NC	909.8	776.8	133.0	0.249
Fe_g-NC/Phen	829.4	583.2	246.2	0.240
Fe_g-NC/Bipy	1025.7	819.9	205.8	0.285

Table S2. XPS data for the surface N species of different catalysts.

Samples	Binding Energy (eV) and atom content percentage (%)			
	Pyridinic-N	**Pyrrrolic-N**	**Graphitic-N**	**Oxidic-N**
	398.20 eV	398.90 eV	400.66 eV	402.59 eV
NC	29.77	22.17	38.78	9.28
NC/Phen	34.90	16.43	45.33	3.34
NC/Bipy	32.34	15.19	45.24	7.23

Table S3. XPS data for the surface species for the bulk species of different catalysts.

Samples	C / wt%	N / wt%	O / wt%	Fe / wt%	Zn / wt%
ZIF8	37.95	21.14	4.87	/	36.05
ZIF8/Phen	46.97	19.20	6.10	/	27.74
NC	78.11	7.86	5.55	/	8.48
NC/Phen	74.02	8.79	7.46	/	9.73
NC/Bipy	76.15	9.59	8.42	/	5.85
Fe_g-NC	78.61	7.34	6.81	3.36	3.88
Fe_g-NC/Phen	78.72	8.62	5.83	4.19	2.65
Fe_g-NC/Phen-20nm	79.71	8.96	5.07	3.44	2.82
Fe_g-NC/Phen-40nm	81.87	8.61	4.65	2.52	2.35
Fe_g-NC/Phen-600	72.09	8.78	7.21	2.23	9.69
Fe_g-NC/Phen-700	76.28	8.77	5.99	2.26	6.71
Fe_g-NC/Phen-850	79.27	8.86	5.59	3.82	2.46
Fe_g-NC/Bipy	78.47	8.25	8.53	2.44	2.31
Fe_I-NC/Phen	80.56	5.94	8.62	1.57	3.31

The atomic percentage (at%) measured by XPS to the weight percentage (wt%) by following equation:

$$x\ wt\% = \frac{M_x \times x\ (at\%)}{12.01 \times C\ (at\%) + 14.01 \times N\ (at\%) + 16.00 \times O\ (at\%) + 65.38 \times Zn\ (at\%) + 5}$$

Where 12.01, 14.01, 16.00, 65.38 and 55.85 are the atomic mass of Fe, O, N, and C, respectively.

Table S4. ICP-MS analysis for different samples.

Samples	**Fe / wt%**	**Zn / wt%**
NC/Phen	/	2.15
NC/Bipy	/	2.43
Fe_g-NC	1.28	0.56
Fe_g-NC/Phen	1.84	0.07
Fe_g-NC/Phen after ADT	1.26	/
Fe_g-NC/Bipy	1.59	0.22
Fe_I-NC/Phen	1.51	1.63
Fe_g-NC/Phen-40mg	1.14	0.67
Fe_g-NC/Phen-70mg	2.15	0.10

Table S5. Structural parameters of NC/Phen extracted from the EXAFS fitting.

Sample	Shell	*N*[a]	*R*(Å)[b]	$\sigma^2\times10^3$(Å^2)[c]	ΔE_0 (eV)[d]	*R* factor
Zn foil	Zn-Zn	6*	2.64±0.01	9.2±1.2	2.4±1.3	0.004
	Zn-Zn	6*	2.78±0.01	18.5±4.1		
ZnO	Zn-O	4.1±0.6	1.96±0.01	4.0±1.3	4.5±1.8	0.012
	Zn-Zn	11.2±1.8	3.23±0.01	12.6±1.2	2.9±1.4	
ZnPc	Zn-N	4.3±0.7	2.00±0.01	3.0±1.2	11.2±2.4	0.007
	Zn-C	6.6±2.5	3.00±0.02	2.5±2.8	12.0±3.2	
NC/Phen	Zn-N	4.1±0.5	2.01±0.01	11.9±1.6	1.9±1.2	0.013

[a]*N*: coordination numbers; [b]R: bond distance; [c]σ^2: Debye-Waller factors; [d]ΔE_0: the inner potential correction. *R* factor: goodness of fit.

Table S6. Comparison of ORR performance of Fe_g-NC/Phen with other reported M-N-C catalysts.

Catalyst	$E_{1/2}$ /V *vs.* RHE	Catalyst loading / mg cm^{-2}	J_k@0.82V / A g^{-1}	Ref.
Fe_g-NC/Phen	**0.840**	**0.6**	**22.50**	**This work**
1.5Zn-ZIF	0.880	0.8	21.97	[1]
(Fe,Co)/N-C	0.863	1.095	9.37	[2]
FeCo-OMPC	0.851	0.6	22.57	[3]
M/FeCo-SAs-N-C	0.851	0.6	22.03	[4]
Fe-ZIF	0.850	0.8	12.14	[5]
Fe/N/C(4mIm)-OAc	0.844	0.6	23.84	[6]
Fe-N-C-3HT-2AL	0.840	0.8	12.55	[7]
Co-N-C@F127	0.840	0.8	9.39	[8]
Fe/N/C-SCN	0.836	0.6	11.30	[9]
TPI@Z8(SiO_2)-650-C	0.823	0.4	15.33	[10]
(Fe,Mn)-N-C	0.820	0.8	-	[11]
PmPDA-FeNx/C	0.820	0.6	-	[12]
pCNT@Fe1.5@GL	0.818	0.2	-	[13]
Fe2-Z8-C	0.805	0.4	-	[14]
Fe-NC-Phen-PANI	0.800	0.6	-	[15]

References

[1] H. Zhang, H. T. Chung, D. A. Cullen, S. Wagner, U. I. Kramm, K. L. More, P. Zelenay, G. Wu, *Energy Environ. Sci.* **2019**, 12, 2548.

[2] J. Wang, Z. Huang, W. Liu, C. Chang, H. Tang, Z. Li, W. Chen, C. Jia, T. Yao, S. Wei, Y. Wu, Y. Li, *J. Am. Chem. Soc.* **2017**, 139, 17281.

[3] J. Y. Cheon, T. Kim, Y. Choi, H. Y. Jeong, M. G. Kim, Y. J. Sa, J. Kim, Z. Lee, T. H. Yang, K. Kwon, O. Terasaki, G. G. Park, R. R. Adzic, S. H. Joo, *Sci. Rep.* **2013**, 3, 2715.

[4] S. H. Yin, J. Yang, Y. Han, G. Li, L. Y. Wan, Y. H. Chen, C. Chen, X. M. Qu, Y. X. Jiang, S. G. Sun, *Angew. Chem. Int. Ed.* **2020**, 59, 21976.

[5] H. Zhang, S. Hwang, M. Wang, Z. Feng, S. Karakalos, L. Luo, Z. Qiao, X. Xie, C. Wang, D. Su, Y. Shao, G. Wu, *J. Am. Chem. Soc.* **2017**, 139, 14143.

[6] Y. Li, P. Zhang, L. Wan, Y. Zheng, X. Qu, H. Zhang, Y. Wang, K. Zaghib, J. Yuan, S. Sun, Y. Wang, Z. Zhou, S. Sun, *Adv. Funct. Mater.* **2021**, 31, 2009645.

[7] N. R. Sahraie, U. I. Kramm, J. Steinberg, Y. Zhang, A. Thomas, T. Reier, J. P. Paraknowitsch, P. Strasser, *Nat. Commun.* **2015**, 6, 8618.

[8] Y. He, S. Hwang, D. A. Cullen, M. A. Uddin, L. Langhorst, B. Li, S. Karakalos, A. J. Kropf, E. C. Wegener, J. Sokolowski, M. Chen, D. Myers, D. Su, K. L. More, G. Wang, S. Litster, G. Wu, *Energy Environ. Sci.* **2019**, 12, 250.

[9] Y. C. Wang, Y. J. Lai, L. Song, Z. Y. Zhou, J. G. Liu, Q. Wang, X. D. Yang, C. Chen, W. Shi, Y. P. Zheng, M. Rauf, S. G. Sun, *Angew. Chem. Int. Ed.* **2015**, 54, 9907.

[10] X. Wan, X. Liu, Y. Li, R. Yu, L. Zheng, W. Yan, H. Wang, M. Xu, J. Shui, *Nat. Catal.* **2019**, 2, 259.
[11] Q. Wang, Z. Y. Zhou, Y. J. Lai, Y. You, J. G. Liu, X. L. Wu, E. Terefe, C. Chen, L. Song, M. Rauf, N. Tian, S. G. Sun, *J. Am. Chem. Soc.* **2014**, 136, 10882.
[12] S. H. Ahn, X. Yu, A. Manthiram, *Adv. Mater.* **2017**, 29, 1606534.
[13] Q. Liu, X. Liu, L. Zheng, J. Shui, *Angew. Chem. Int. Ed.* **2018**, 57, 1204.
[14] X. Fu, P. Zamani, J. Y. Choi, F. M. Hassan, G. Jiang, D. C. Higgins, Y. Zhang, M. A. Hoque, Z. Chen, *Adv. Mater.* **2017**, 29, 1604456.

Table S7. Comparison of H_2–O_2 PEMFCs activity of Fe_g-NC/Phen with other reported M-N-C catalysts.

Catalysts	J@0.9$V_{iR\text{-free}}$ / A cm^{-2}	J@0.8$V_{iR\text{-free}}$ / A cm^{-2}	P_{max} / W cm^{-2}	Absolute Pressure / bar	Loading / mg cm^{-2}	Year	Ref.
Fe_g-NC/Phen	**0.046 (2bar)**	**0.509**	**1.53/1.22**	**2.5/1.5**	**3.5**	**22**	**This work**
Fe/N/C(4mIm)-OAc	0.009 (1bar)	0.320 (2bar)	1.33/1.12	2.5/1.5	3.0	21	[1]
Fe-MOF100nm	0.029 (1bar)	0.150 (1bar)	1.14	1.7	4.0	20	[2]
TPI@Z8(SiO_2)-650-C	0.022 (1bar)	0.560 (2.5bar)	1.18	2.5	2.7	19	[3]
Fe2-Z8-C	0.014 (1bar)	0.081 (1bar)	1.14	2.5/2	2.8	17	[4]
(Fe,Co)/N-C	/	/	0.98/0.85	2/1	0.77	17	[5]
CNT/Fe-ZIF-p	/	~0.220 (1bar)	0.82	1.5	4.5	17	[6]
GNP_25_1	/	~0.090 (0bar)	0.52	0.5	4	16	[7]
Fe-N-C-Phen-PANI	/	0.390 (2bar)	1.06	2.5	4.0	16	[8]
Fe/N/C-SCN	/	0.380 (2bar)	1.03/0.94	2.5/1.5	4.0	15	[9]
ZIF-8/TPI	/	/	0.62	1.5	2.2	14	[10]
PFeTTPP-1000	/	0.157 (1bar)	0.73	1.5	4.1	13	[11]
Fe/TPTZ/ZIF-8	/	/	0.75	1.5	4	13	[12]
Fe/Phen/Z8	0.008 (1bar)	0.287 (1bar)	0.91	1.5	3.90	2011	[13]

References

[1] Y. Li, P. Zhang, L. Wan, Y. Zheng, X. Qu, H. Zhang, Y. Wang, K. Zaghib, J. Yuan, S. Sun, Y. Wang, Z. Zhou, S. Sun, *Adv. Funct. Mater.* **2021**, 31, 2009645.

[2] A. Uddin, L. Dunsmore, H. Zhang, L. Hu, G. Wu, S. Litster, *ACS Appl. Mater. Interfaces.* **2020**, 12, 2216.

[3] X. Wan, X. Liu, Y. Li, R. Yu, L. Zheng, W. Yan, H. Wang, M. Xu, J. Shui, *Nat. Catal.* **2019**, 2, 259.

[4] Q. Liu, X. Liu, L. Zheng, J. Shui, *Angew. Chem. Int. Ed.* **2018**, 57, 1204.

[5] J. Wang, Z. Huang, W. Liu, C. Chang, H. Tang, Z. Li, W. Chen, C. Jia, T. Yao, S. Wei, Y. Wu, Y. Li, *J. Am. Chem. Soc.* **2017**, 139, 17281.

[6] C. Zhang, Y. C. Wang, B. An, R. Huang, C. Wang, Z. Zhou and W. Lin, *Adv. Mater.*, **2017**, 29, 1604556.

[7] Y. Yao, Y. You, G. Zhang, J. Liu, H. Sun, Z. Zou and S. Sun, *ACS Appl. Mater. Interfaces*, **2016**, 8, 6464-6471.

[8] X. Fu, P. Zamani, J. Y. Choi, F. M. Hassan, G. Jiang, D. C. Higgins, Y. Zhang, M. A. Hoque, Z. Chen, *Adv. Mater.* **2017**, 29, 1604456.
[9] Y. C. Wang, Y. J. Lai, L. Song, Z. Y. Zhou, J. G. Liu, Q. Wang, X. D. Yang, C. Chen, W. Shi, Y. P. Zheng, M. Rauf, S. G. Sun, *Angew. Chem. Int. Ed.* **2015**, 54, 9907.
[10] D. Zhao, J. L. Shui, L. R. Grabstanowicz, C. Chen, S. M. Commet, T. Xu, J. Lu and D. J. Liu, *Adv. Mater.*, **2014**, 26, 1093-1097.
[11] S. Yuan, J.-L. Shui, L. Grabstanowicz, C. Chen, S. Commet, B. Reprogle, L. Y. Tao Xu and a. D.-J. Liu, *Angew. Chem. Int. Ed.*, **2013**, 125, 8507-8511.
[12] J. Tian, A. Morozan, M. T. Sougrati, M. Lefevre, R. Chenitz, J. P. Dodelet, D. Jones and F. Jaouen, *Angew. Chem. Int. Ed.*, **2013**, 52, 6867-6870.
[13] E. Proietti, F. Jaouen, M. Lefevre, N. Larouche, J. Tian, J. Herranz, J. P. Dodelet, *Nat. Commun.* **2011**, 2, 416.

Table S8. Comparison of H_2–air PEMFCs activity of Fe_g-NC/Phen with other reported M-N-C catalysts.

Catalyst	P_{max} / W cm^{-2}	J@0.8V / mA cm^{-2}	J@0.8V$_{iR\text{-}free}$ / mA cm^{-2}	Abs Pressure / bar	Catalyst loading / mg cm^{-2}	Ref.
Fe_g-NC/Phen	**0.711**	**120.8**	**160**	**1**	**3.5**	**This work**
Fe-MOF catalyst	0.61	/	~120*	1.0	4.0	[1]
SA-FeNx-ZIF8-PCM	0.60	~100*	~170*	1.9	2.7	[2]
NPMC (CA#1)	0.57	~80*	~120*	1..74	4.0	[3]
Mn−N−C−S	~0.500	~80*	~90	2	4	[4]
(Fe,Co)/N-C	0.505	54*	54*	2	0.77	[5]
Fe/N/C(4mIm)-OAc	0.467	~40*	~50*	1	3.0	[6]
TPI@Z8(SiO_2)-650-C	0.42	105	129	1	2.0	[7]
(CM+PANI)-Fe-C	0.42	75	90	1	4	[8]
FePhenMOF-$ArNH_3$	~0.4	~50*	~50	2.5	2	[8]
Fe-N-C-Phen-PANI	0.38	85*	120	1.88	4	[9]
FePhen@MOF-$ArNH_3$	0.38	50	50	2	3	[10]
Co(mIm)-NC(1.0)	~0.32	~30*	~76	1	6.3	[11]
Fe-MOF-700/1000	0.302	~30*	30*	1.5	4	[12]

*These values are not directly given in the papers, thus obtained by digging the polarization curves or calculated by the data provided.

References

[1] A. Uddin, L. Dunsmore, H. Zhang, L. Hu, G. Wu, S. Litster, *ACS Appl. Mater. Interfaces.* **2020**, 12, 2216.

[2] X. Fu, R. Gao, G. Jiang, M. Li, S. Li, D. Luo, Y. Hu, Q. Yuan, W. Huang, N. Zhu, L. Yang, Z. Mao, J. Xiong, A. Yu, Z. Chen, Z. Bai, *Nano Energy* **2021**, 83, 105734.

[3] Dustin Banham, Takeaki Kishimoto, Yingjie Zhou, Tetsutaro Sato, Kyoung Bai, Jun-ichi Ozaki, Yasuo Imashiro, S. Ye*, *Sci. Adv.* **2018**, 4, 7180.

[4] L. Guo, S. Hwang, B. Li, F. Yang, M. Wang, M. Chen, X. Yang, S. G. Karakalos, D. A. Cullen, Z. Feng, G. Wang, G. Wu, H. Xu, *ACS Nano* **2021**, 15, 6886.

[5] J. Wang, Z. Huang, W. Liu, C. Chang, H. Tang, Z. Li, W. Chen, C. Jia, T. Yao, S. Wei, Y. Wu, Y. Li, *J. Am. Chem. Soc.* **2017**, 139, 17281.

[6] Y. Li, P. Zhang, L. Wan, Y. Zheng, X. Qu, H. Zhang, Y. Wang, K. Zaghib, J. Yuan, S. Sun, Y. Wang, Z. Zhou, S. Sun, *Adv. Funct. Mater.* **2021**, 31, 2009645.
[7] X. Wan, X. Liu, Y. Li, R. Yu, L. Zheng, W. Yan, H. Wang, M. Xu, J. Shui, *Nat. Catal.* **2019**, 2, 259.
[8] Hoon T. Chung, David A. Cullen, Drew Higgins, Brian T. Sneed, Edward F. Holby, Karren L. More, P. Zelenay*, *Science* **2017**, 357, 479.
[9] X. Fu, P. Zamani, J. Y. Choi, F. M. Hassan, G. Jiang, D. C. Higgins, Y. Zhang, M. A. Hoque, Z. Chen, *Adv. Mater.* **2017**, 29, 1604456.
[10] K. Strickland, E. Miner, Q. Jia, U. Tylus, N. Ramaswamy, W. Liang, M. T. Sougrati, F. Jaouen, S. Mukerjee, *Nat. Commun.* **2015**, 6, 7343.
[11] X. Xie, C. He, B. Li, Y. He, D. A. Cullen, E. C. Wegener, A. J. Kropf, U. Martinez, Y. Cheng, M. H. Engelhard, M. E. Bowden, M. Song, T. Lemmon, X. S. Li, Z. Nie, J. Liu, D. J. Myers, P. Zelenay, G. Wang, G. Wu, V. Ramani, Y. Shao, *Nat. Catal.* **2020**, 3, 1044.
[12] F. Afsahi, S. Kaliaguine, *J. Mater. Chem. A* **2014**, 2, 12270.

Table S9. Structural parameters of Fe_g-NC/Phen extracted from the EXAFS fitting.

Sample	Shell	N^a	R(Å)^b	$\sigma^2\times10^3$(Å^2)^c	ΔE_0 (eV)^d	R factor
Fe foil	Fe-Fe	8*	2.47±0.01	5.0±0.4	7.1±0.7	0.002
	Fe-Fe	6*	2.84±0.01	6.5±0.8	5.5±1.7	
Fe_2O_3	Fe-O	6.2±1.3	1.93±0.02	11.7±2.3	-5.7±3.0	0.012
	Fe-Fe	4.6±2.4	2.98±0.02	8.8±5.0	-4.2±1.2	
FePc	Fe-Fe	8.5±4.5	3.42±0.02	10.3±3.2	-7.9±3.3	0.007
	Fe-N	4.0±0.5	1.97±0.02	7.2±3.1	6.0±4.1	
Fe_g-NC	Fe-N	4.4±0.9	2.00±0.02	14.5±2.9	-2.4±2.1	0.009
Fe_g-NC/Phen	Fe-N	4.2±0.8	2.01±0.02	13.7±2.8	0.5±2.1	0.016
Fe_g-NC/Bipy	Fe-N	3.7±0.5	2.02±0.01	11.1±1.8	2.9±1.3	0.004

$^a N$: coordination numbers; $^b R$: bond distance; $^c\sigma^2$: Debye-Waller factors; ^{d} ΔE_0: the inner potential correction. R factor: goodness of fit.

Table S10. Average Mössbauer parameters of different samples.

Samples	Comp.	RA %	IS mm s^{-1}	QS mm s^{-1}	LW mm s^{-1}	H Tesla	Assignment
Fe_g-NC	D1	80.33	0.1176	0.5505	0.6405	/	O_2-$Fe^{III}N_4$
	D2	19.67	0.4375	1.3750	0.9330	/	MS $Fe^{II}N_4$
Fe_I-NC/Phen	D1	83.54	0.1250	0.5893	0.6768	/	O_2-$Fe^{III}N_4$
	D2	16.46	0.4730	1.2184	0.7767	/	MS $Fe^{II}N_4$
Fe_g-NC/Phen	D1	92.14	0.1250	0.4911	0.6447	/	O_2-$Fe^{III}N_4$
	D2	7.86	0.3750	1.7679	0.8880	/	MS $Fe^{II}N_4$
Fe_g-NC/Phen at 23 K	D1	36.14	0.3598	0.4911	0.6580	/	O_2-$Fe^{III}N_4$
	D2	63.64	0.3845	1.6696	0.9582	/	MS $Fe^{II}N_4$
Fe_g-NC/Phen-70mg	D1	33.76	0.1250	0.4911	0.7040	/	O_2-$Fe^{III}N_4$
	D2	3.65	0.4719	2.0339	0.6339	/	MS $Fe^{II}N_4$
	Sext 1	48.15	-0.2131	-0.0069	0.7718	34.07	Alpha-iron
	Sext 2	14.44	0.2041	0.0242	0.4925	34.02	Iron carbide

Table S11. O_2 adsorption energies (E_{ads}, eV), O-O bond lengths (d_{O-O}), Fe-O bond lengths (d_{Fe-O}) and Fe-N bond lengths (Å) before O_2 adsorption (d_{Fe-N}) of Fe_g-NC and Fe_g-NC/Phen.

Samples	E_{ads} (eV)	d_{Fe-N} (Å)	d_{O-O} (Å)	d_{Fe-O} (Å)
Fe_g-NC	-0.416	1.979	1.282	1.997
Fe_g-NC/Phen	-0.481	1.997	1.287	1.979

Table S12. Summary of catalyst SD, TOF and iron utilization determined by the nitrite stripping experiment.

Catalysts	Q_{strip} / C g^{-1}	SD / μmol g^{-1}	TOF@0.85V / s^{-1}	Fe contents / wt%	Fe utilization
Fe_g-NC/Phen	45.46	94.23	2.01	1.84	28.60
Fe_g-NC/Bipy	37.19	77.08	2.29	1.59	27.07
Fe_I-NC/Phen	25.18	52.19	2.74	1.51	19.30
Fe_g-NC	17.03	35.30	1.64	1.28	15.40